Rock Mechanics and Rock Engineering
https://doi.org/10.1007/s00603-025-04748-6

ORIGINAL PAPER

Thermal Effects on the Generalized Mode III Fracture Behavior of Transversely Isotropic Sandstone: A Study Using Acoustic Emission Localization and 3D Scanning Reconstruction

Xiaofeng Qin[1] · Haijian Su[1] · Liyuan Yu[1] · Thi Nhan Pham[2] · Enzhuo Zhao[1] · Menglong Zhang[1]

Received: 12 December 2024 / Accepted: 26 June 2025

Abstract

The generalized mode III fracture loading was conducted on edge notch disc bend sandstone specimens with three bedding configurations after thermal treatment at temperatures ranging from 75 to 600 °C. The influences and underlying mechanisms of thermal and bedding effects on mode III fracture behavior were analyzed based on acoustic emission (AE) localization and 3D scanning reconstruction techniques. The results demonstrate that the spatial relationship between bedding planes and the prefabricated notch significantly influences the strength and fracture characteristics. Specifically, specimens with short-transverse configuration exhibit lower peak loads (12.00% lower than divider configuration), reduced fracture energy (the initial fracture energy and peak fracture energy are 56.32% and 23.49% lower, respectively, than divider configuration), and lower stress intensity factors (the initial stress intensity factor and peak stress intensity factor are 22.82% and 13.37% lower, respectively, than divider configuration), making crack initiation more likely. Thermal effects also influence mode III fracture behavior, as both the stress intensity factors and fracture energy gradually decrease with increasing thermal treatment temperature. Furthermore, the high-temperature (400–600 °C) treatments tend to mitigate the influence of bedding configurations. The medium-amplitude (50–70 dB) and high-amplitude (70–90 dB) AE signals are critical indicators of mode III crack initiation and propagation. Temporally, these signals predominantly occur as sustained events during the crack propagation and macroscopic failure stages following crack initiation. Spatially, the medium-amplitude and high-amplitude signals are primarily concentrated near the prefabricated notch. In contrast, the low-amplitude (30–50 dB) signals caused by pore closure and grain friction are widely distributed throughout the entire duration and spatial extent of the tests.

Highlights

- The generalized mode III stress intensity factor was calculated, considering the effects of transverse isotropy.
- The effect of transverse isotropy and thermal treatment on mode III fracture behavior was analyzed.
- The mode III fracture propagation mechanism was discussed based on AE localization techniques.
- The fracture surface was reconstructed using 3D scanning to analyze spatial crack propagation.
- The out-of-plane crack propagation characteristics were quantitatively analyzed.

Keywords Generalized mode III fracture · Transverse isotropy · Thermal effect · AE localization · 3D scanning

✉ Haijian Su
hjsu@cumt.edu.cn

[1] State Key Laboratory of Intelligent Construction and Healthy Operation and Maintenance of Deep Underground Engineering, China University of Mining and Technology, Xuzhou 221116, China

[2] Faculty of Civil Engineering, Hanoi University of Mining and Geology, Hanoi 100000, Vietnam

Published online: 08 August 2025

Abbreviations

a	Depth of prefabricated notch
B	Thickness of ENDB specimen
D_f	Fractal dimension
E, E'	Elastic modulus of rock
G, G'	Shear modulus of rock
K, K_I, K_{II}, K_{III}, $K_{III\text{-isotropy}}$, $K_{III\text{-anisotropy}}$	Stress intensity factor
P	Applied load
R	Radius of ENDB specimen
$2S$	Span of the lower support
v, v'	Poisson's ratio of rock
W_a, W_i	Fracture energy
$Y_{III\text{-isotropy}}$, $Y_{III\text{-anisotropy}}$	Geometry factor
γ	Crack initiation angle
δ	Final rupture angle

1 Introduction

The fracture mechanical properties of rock are of significant importance in rock engineering, especially in fields such as geothermal energy development and deep geological disposal of nuclear waste (Hanano 2004; Saceanu et al. 2022; Zhao et al. 2024b). In geothermal energy development, high-temperature environments may induce crack propagation in rocks, affecting the stability and permeability of reservoirs (Hanano 2004; Feng et al. 2020). In nuclear waste disposal, the thermal effects caused by radioactive decay may induce rock mass fracturing, threatening the long-term safety of underground repositories (Min et al. 2005; Saceanu et al. 2022). As underground engineering advances into deeper and high-temperature complex environments, accurately understanding the fracture behavior of rock is crucial for underground energy resources extraction and deep subsurface space utilization.

During the formation and existence of rock, under the influence of internal and external forces (such as changes in the mineral crystal structure and alignment direction, geological structural deformation, stress history, and depositional environment), various types and scales of structural features (including foliation, bedding, joints, fractures, faults) and pores are generated (Hargraves et al. 1991; Barton and Quadros 2015). These inherent heterogeneities cause the physical and mechanical properties of rocks to vary with direction, resulting in pronounced anisotropic characteristics (Zeng et al. 2008; Ghazvinian et al. 2013). Sun et al. (2024) reported that the fracture toughness of coal rocks exhibits significant anisotropy, with mode I fracture toughness increasing as the bedding angle increases. Zhou et al. (2023) conducted hydraulic fracturing tests on hollow double-wing crack Longmaxi shale specimens with three different main crack orientations. They found that both mode I fracture toughness and fracture energy demonstrated strong anisotropy under different confining pressures. Ma et al. (2023) performed mode I fracture loading on notched semi-circular bend shale specimens with different bedding angles, and observed that cracks tended to propagate along the bedding planes when the bedding angle was small. Fan et al. (2022) reported that mode II fracture toughness in shale exhibits significant anisotropy. Using digital image correlation (DIC) technology, they identified a dominant high-strain zone along the prefabricated crack direction and a secondary high-strain zone along the bedding direction. Chen et al. (2023) further demonstrated that the development of the fracture process zone is also influenced by rock anisotropy based on DIC analysis. Similar reports include the anisotropy of mixed mode I-II fractures in Longmaxi shale and metamorphic granite (Wang et al. 2020; Sakha et al. 2022), the anisotropy of mode I fractures in coal rocks and layered phyllite under dynamic loading (Chang et al. 2022; Shi et al. 2022), and the anisotropy of mixed mode I-III fractures in layered limestone (Liu et al. 2023), among others.

Sedimentary rocks are among the most common types of crustal rocks, and their transverse isotropy can be regarded as a specific case of anisotropy. As a typical sedimentary rock, sedimentary sandstone exhibits significant differences in mechanical properties between the in-plane and out-of-plane directions due to its layered structure or depositional characteristics. This anisotropy results in complex changes in crack propagation paths and stress distribution (Nejati et al. 2021; Zheng et al. 2023a). In transversely isotropic rock, cracks tend to propagate along certain preferred directions, presenting new challenges for the study of fracture behavior. Liu et al. (2024) conducted loading tests on cracked straight-through Brazilian disc sandstone with layered characteristics and summarized three typical crack propagation patterns in the in-plane direction: bedding-parallel propagation, matrix propagation, and a mixed-mode propagation. Roy et al. (2017) conducted loading experiments on sandstone specimens with various bedding combinations and found that fracture toughness is positively correlated with bedding spacing, whereas the length of the fracture process zones is negatively correlated with bedding spacing.

In addition, thermal effects are also a critical factor influencing the fracture mechanical behavior of rock. High-temperature environments can induce heterogeneous thermal expansion among minerals within sandstone, leading to the formation of thermal cracks and resulting in changes to both the microstructure and macroscopic mechanical properties of the rock (Yin et al. 2012; Miao et al. 2020; Jiang et al. 2023). After thermal treatment, the strength and elastic modulus of rocks may undergo significant changes, and the mechanisms of crack initiation and propagation may also change accordingly (Yin et al. 2021; Su et al. 2022; Alneasan

et al. 2022; Shi et al. 2023). Therefore, the fracture behavior of layered rock masses becomes more complex under high-temperature environments. Weng et al. (2024) reported that high temperatures significantly reduced the anisotropy of strength in layered rocks. Xi et al. (2024) reported the influence of thermal effects on the anisotropy of dynamic tensile strength. Zhou et al. (2024) conducted direct shear tests on shale with varying bedding angles after thermal treatment and found that the thermal effect enhanced the propagation of shear-induced cracks along the bedding planes. Shang et al. (2019), through numerical simulations, explored the influence of thermal effects on the fracture behavior of in-plane cracks in anisotropic rocks.

Although some researchers have focused on the influence of thermal effects on the fracture behavior of anisotropic rock masses, current studies primarily concentrate on the fracture behavior of in-plane cracks (mode I, mode II, and mixed mode I-II) in rocks. In contrast, investigations on out-of-plane shear (mode III) cracks remains relatively limited. Therefore, this work aims to explore the influence of thermal effects on the mode III fracture behavior of transversely isotropic sandstone. Edge notch disc bend (ENDB) sandstone specimens with three different bedding configurations were subjected to thermal treatment at temperatures ranging from 75 to 600 °C, followed by generalized mode III fracture loading. The influence of thermal effects and anisotropic characteristics on mode III fracture behavior was analyzed from the perspectives of strength, fracture characteristics, and energy characteristics. Additionally, based on acoustic emission (AE) and 3D scanning reconstruction techniques, the characteristics of fracture signals and fracture surface morphology were quantitatively analyzed. Furthermore, the crack propagation mechanism was discussed based on AE localization.

2 Materials and Methods

2.1 Methodology of Mode III Fracture in Isotropic Materials

Applying a loading with a certain deflection angle β to ENDB specimens (Fig. 1a) is a common method for achieving mode III fracture loading (Aliha et al. 2023; Zheng et al. 2024; Shi et al. 2024; Shui et al. 2024; Wang et al. 2024). The values of stress intensity factors (K_{I}, K_{II}, and K_{III}, SIFs) under different loading angles can be calculated using the finite element method with Abaqus software to determine the deflection angle β and the geometry factor Y for pure mode III fracture (Pietras et al. 2023; Aliha et al. 2023; Shui et al. 2024). The mode III stress intensity factor can be calculated using Eq. (1).

$$K_{\text{III-isotropy}} = \frac{3PS}{2RB^2}\sqrt{\pi a}Y_{\text{III-isotropy}}\left(\frac{a}{B}, \frac{S}{R}, \beta\right) \tag{1}$$

where P is the applied load, R and $2S$ are the radius of the specimen and the span of the lower support, respectively. B and a represent the thickness of the specimen and the depth of the prefabricated notch, respectively. For isotropic materials, the value of $Y_{\text{III-isotropy}}$ depends only on a/B, S/R, and β.

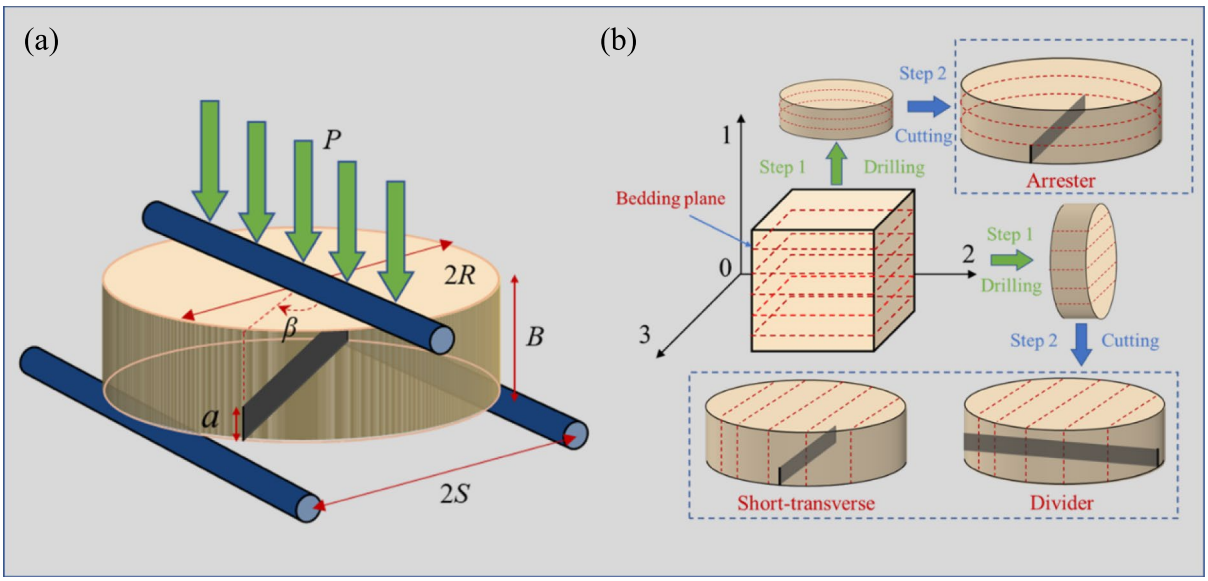

Fig. 1 Schematic diagram of ENDB specimen: **a** Geometry and dimensions; **b** preparation of ENDB specimens with three bedding configurations

2.2 Lithology and Size

All specimens used in this work were extracted from the same sandstone block collected from the Wuding County, Chuxiong Yi Autonomous Prefecture, Yunnan Province, China. The sandstone exhibits well-developed bedding, with uniformly spaced bedding planes approximately 2–4 mm apart and an average density of approximately 2224 kg/m^3. According to the X-ray diffraction (XRD) results (in Fig. 2a), the sandstone is primarily composed of quartz, potassium feldspar, calcite, and illite. The main difference between the matrix and bedding lies in the relative mineral composition: the bedding contains a higher content of calcite and illite compared to the matrix. Under the microscope (in Fig. 2b), the grain size distribution of the rock is observed to range from 0.05 to 0.25 mm. The mineral grains are cemented in a tightly interlocked (mosaic-like) manner, and the bonding between the bedding and the matrix is dense and continuous.

The use of ENDB specimens for mode III fracture loading has been widely applied in the fracture mechanics research of materials such as asphalt, concrete, gypsum, and homogeneous rocks (Ahmadi et al. 2021; Aliha et al. 2023; Liu et al. 2023; Karimi et al. 2024). Based on the practical experience from these previous studies and considering specimen manufacturability, the final specimen dimensions were selected as follows: radius $R=50$ mm, thickness $B=30$ mm, span ratio $S/R=0.95$, and notch depth ratio $a/B=0.4$. As shown in Fig. 1b, the parent sandstone rock was first cut into several cubic specimens with edge lengths of 110 mm. Then, two types of cylindrical specimens with a diameter of 100 mm were drilled from different orientations using a core drill machine. The drilled cylindrical specimens were subsequently sliced into smaller cylinders with a thickness of 30 mm using wire cutting. To produce transversely isotropic ENDB sandstone specimens with different notch orientations, three sets of notches (100 mm in length and 12 mm in depth) were introduced through the center of the small cylindrical specimens in accordance with the three bedding-notch configurations recommended by ISRM (Ulusay 2015): Arrester, Short-transverse, and Divider. Specifically, the configuration which the notch depth direction is orthogonal to the bedding plane and the notch front edge is perpendicular to the bedding neutral axis is termed "Arrester"; the configuration with the notch depth direction parallel to the bedding plane is termed "Short-transverse"; and the configuration in which the notch strike direction is orthogonal to the bedding plane and the notch front edge is parallel to the bedding neutral axis is termed "Divider".

2.3 Methodology of Mode III Fracture in Transversely Isotropic Materials

Although the ENDB specimen method for achieving mode III fracture has been widely applied to anisotropic materials, it is often simplified as an isotropic material when calculating the stress intensity factor and solving for the deflection angle and geometry factor (Cao et al. 2024; Zheng et al. 2024; Wang et al. 2024). However, the geometry factor of materials with anisotropic characteristics is significantly influenced by their anisotropic features (Ren et al. 2021; Wang et al. 2020; Liu et al. 2023). Therefore, based on the implementation of mode III fracture using isotropic ENDB specimens, this work takes into account the true transverse isotropic characteristics of the material. The generalized mode III fracture parameters for the transverse isotropic ENDB specimens were obtained by applying the J-integral method to the crack tip.

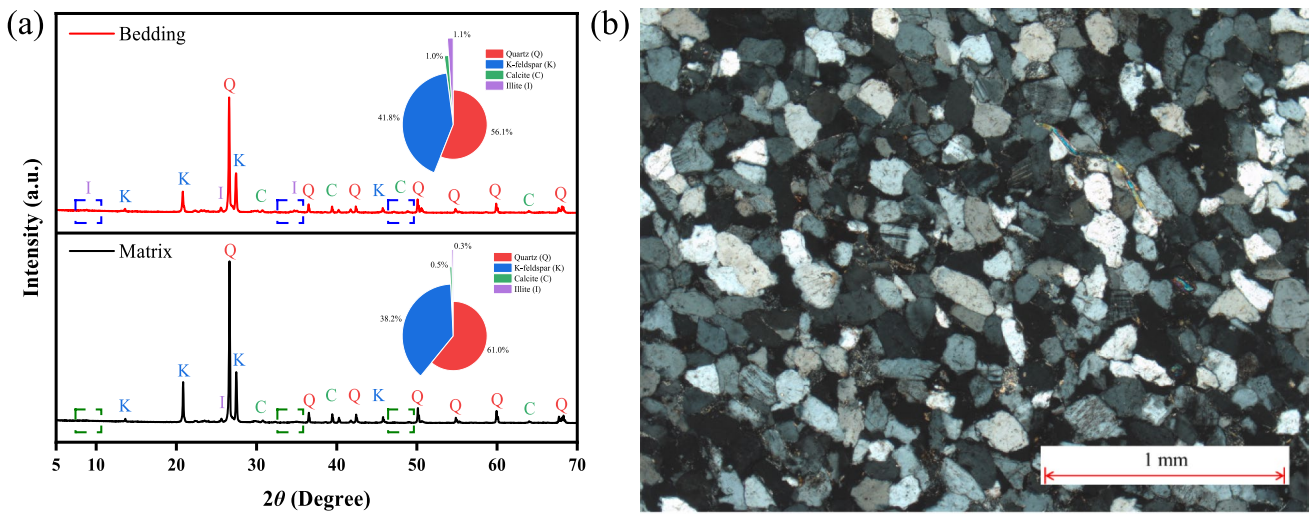

Fig. 2 **a** Xrd and **b** polarizing micrograph test results

The specific details are as follows: An ENDB finite element model with the same dimensions was constructed using Abaqus software, as shown in Fig. 3. The model consists of a total of 89,744 solid C3D20 elements. Based on small strain analysis, the prefabricated notch was assigned through Seam modeling method to simulate crack-tip singularity and accurately calculate stress intensity factors (Shui et al. 2024). The region with the crack front line as the axis was selected as the integration domain (where the crack width near the crack tip of the initial sharp crack in Seam is zero, thus avoiding the issue of non-singular blunt crack tips in the modeling construction). The crack singularity is simulated by folding a face of the 20-node C3D20 element and moving the intermediate node to 1/4 of the edge of the element to form a quarter-point element (Nejati et al. 2015). The mechanical parameters measured from laboratory uniaxial tests (Table 1) were assigned to the model, with the transverse isotropic parameters assigned according to the direction shown in Fig. 3b.

Equation (2) is the generalized mode III fracture stress intensity factor calculation formula that considers transverse isotropic characteristics (Liu et al. 2023). By substituting the mode III stress intensity factor obtained from contour integrals (based on Abaqus software) into the Eq. (3), the geometry factor can be determined. Consequently, the finite element results are obtained as follows: When the deflection angle is 64° (with the constraints of $S/R = 0.95$, $a/B = 0.4$, and the anisotropic parameter as shown in Table 1), generalized mode III fracture occurs. The geometry factors $Y_{\text{III-A}}$, $Y_{\text{III-S}}$, and $Y_{\text{III-D}}$ are 0.2730, 0.2585, and 0.2642, respectively. For isotropic materials, the deflection angle and geometry factor are 65° and 0.2847, respectively.

$$K_{\text{III-anisotropy}} = \frac{3PS}{2RB^2}\sqrt{\pi a}\,Y_{\text{III-anisotropy}}\left(\frac{a}{B}, \frac{S}{R}, \beta, E, E', \nu, \nu', G, G'\right) \tag{2}$$

Table 1 Mechanical properties of ENDB specimens with three bedding configurations

E (GPa)	E'(GPa)	ν	ν'	G'(GPa)
26.734	22.091	0.176	0.255	8.293

$$Y_{\text{III-anisotropy}} = \frac{K_{\text{III - anisotropy}}}{\sqrt{\pi a}} \cdot \frac{2RB^2}{3PS} \tag{3}$$

2.4 Experimental Apparatus and Procedure

The processed specimens were placed in a natural drying environment at room temperature (25 °C) for 48 h. Based on the target heat treatment temperatures, the specimens of the three configurations were grouped into five temperature levels (75 °C, 150 °C, 200 °C, 400 °C, and 600 °C) for heat treatment and one control group without heat treatment (25 °C), with three specimens in each group. The specimens to be heat-treated were placed in a muffle furnace and heated to the target temperature, as shown in Fig. 4a. A constant heating rate of 2 °C/min was applied to increase the temperature from room temperature to the target temperature, followed by isothermal treatment at the target temperature for 4 h to avoid thermal non-uniformity. The specimens were then naturally cooled to room temperature. The processed specimens of each group are shown in Fig. 4b. Due to the physical and chemical changes of the minerals under temperature treatment, the original light-yellow sandstone specimens gradually turned to a reddish-brown color, with the reddish-brown color becoming particularly more prominent along the bedding planes. It is specifically noted that the grain expansion deformation caused by the thermal effect is much smaller than the prefabricated notch and the dimensions of the specimen. Therefore, the volumetric expansion

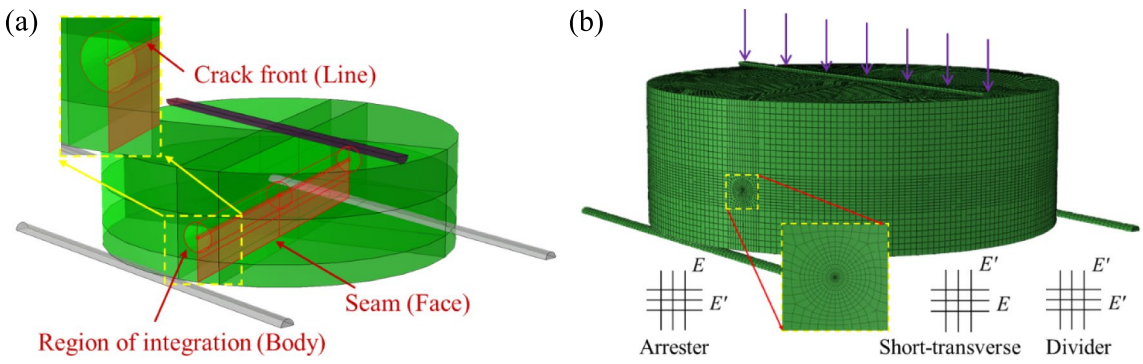

Fig. 3 Finite element simulation of anisotropic ENDB specimen: **a** model modeling, Seam assignment and crack tip setting; **b** grid setting and material property assignment

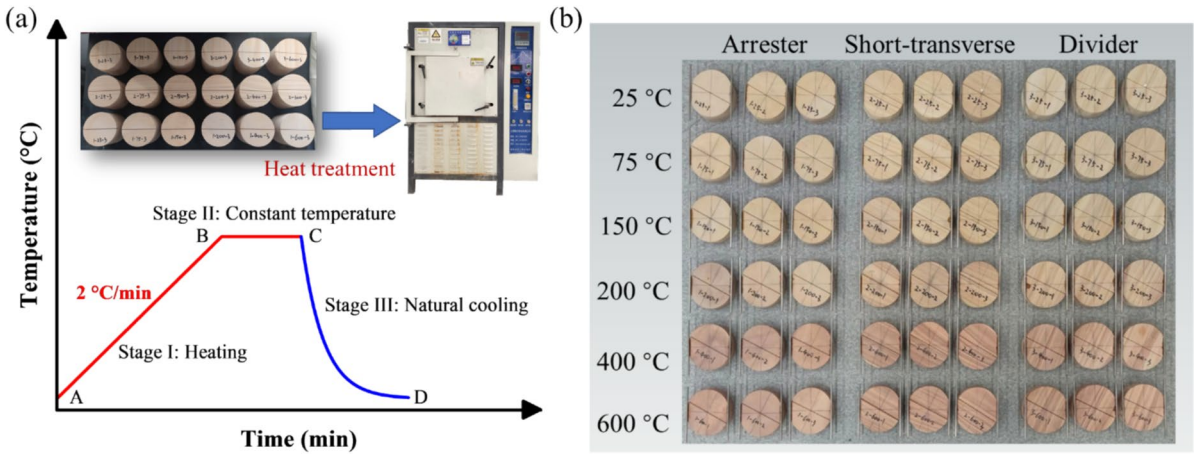

Fig. 4 **a** Heat treatment process of specimens; **b** specimens after heat treatment

caused by high temperature is neglected in this work. In other words, the generalized mode III fracture characteristic parameters calculated at room temperature in Sect. 2.3 are still applicable to the heat-treated specimens. This simplification method has been widely accepted in the literature (Yin et al. 2021; Su et al. 2022; Jiang et al. 2023; Shi et al. 2023; Zhao et al. 2024a).

The experiments were conducted using a FHCA-300 mechanical testing machine (manufactured by GCTS, USA), which has a maximum load capacity of 200 kN and a sensitivity of 0.05%, as shown in Fig. 5a. Before loading, three steel rods (diameter: 4 mm) made of 304 stainless steels were bonded to the top and bottom of the specimen as the upper loading rods and lower support rods, respectively, based on the span and deflection angle. During loading, a displacement-controlled mode was used, applying a constant rate of 0.1 mm/min until specimen failure occurred.

In addition to the displacement and load sensor monitoring, an AE monitoring system (manufactured by Physical Acoustics Corporation, USA) was also used to collect fracture signals during the experiment. The AE monitoring system consists primarily of an AE sensor with a central frequency of 300 kHz, a preamplifier, and a signal acquisition and processing system. The signal acquisition and processing system is based on the AEwin for SAMOS platform, which offers functionalities such as filtering, signal conversion, data collection, and post-processing.

During the test, the time difference of arrival (TDOA) method (Zhao et al. 2021; Liu et al. 2022; Dong et al. 2022) was used to locate the source of fracture signals. Six AE

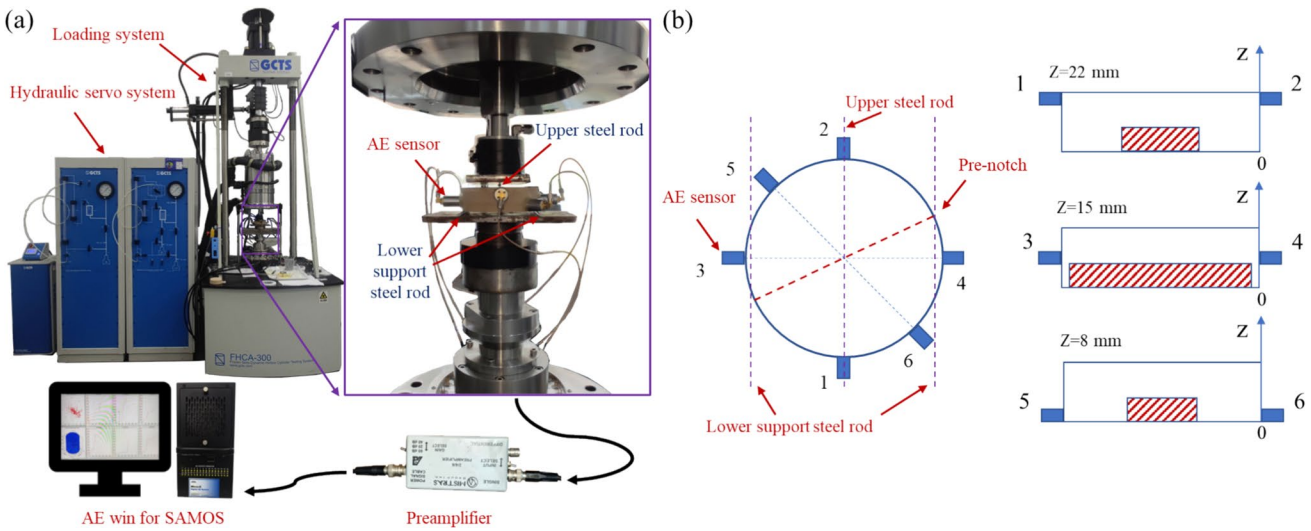

Fig. 5 Specimen loading and monitoring system: **a** schematic diagram of the test system; **b** layout diagram of AE sensors

sensors were arranged into three AE signal localization units and fixed onto the specimen surface according to the spatial configuration shown in Fig. 5b, enabling the determination of AE source positions. Considering the specimen dimensions and wave velocity, the preamplifier was set to 40 dB. The background noise range was determined through the pencil lead break test (Li et al. 2019; Zhao and Liu 2021), with the signal threshold for signal acquisition set to 32 dB. To accurately capture the fracture signals, the digital filter was configured with a signal retention frequency range of 100–400 kHz. Upon the initiation of loading, the electronic signal from the testing machine triggers the AE data acquisition. The acquisition system continuously captures fracture signals at a sampling rate of 1 MSPS (based on the Nyquist sampling theorem Landau 1967; Ren et al. 2023), this rate ensures reliable capture of signals with a maximum frequency of 500 kHz). The captured AE signals are amplified and filtered through the preamplifier and acquisition system, and the source location is determined by calculating the signal arrival time differences at the positioning units.

To quantitatively study the out-of-plane propagation of mode III fracture, the fractured specimens were scanned using a 3D scanner (with a resolution of 50 μm, point accuracy of ± 25 μm, and volume accuracy of ± 50 μm/m). The scanner (developed by Tiertime Co., Ltd., Beijing, China) consists of a measurement system and a post-processing system. The measurement system primarily includes a camera, structure light projector, tripod head and tripod, as illustrated in Fig. 6. The point cloud data of the fracture surface was precisely collected. Based on reference substance, the point cloud data was denoised and fitted to obtain a fitting surface. The surface was then further trimmed to reconstruct the fracture surface. The operation process and the typical reconstructed fracture surface are shown in Fig. 6.

3 Testing Results

3.1 Characteristics of Mode III Fracture Behavior Transversely Isotropic Sandstone

The typical loading curves and peak loads for the unheated ENDB sandstone specimens with three different bedding configurations are shown in Fig. 7. The detailed values were shown in Table 2. Unlike in-plane cracks (mode I, mode II, mixed mode I-II) that are influenced by bedding configurations, the ENDB specimens of transversely isotropic sandstone exhibit two distinct characteristics when experiencing mode III fracture. On the one hand, compared with in-plane fracture loading (data from Aliha et al. 2023; Liu et al. 2023; Shui et al. 2024), the compaction stage of specimens under mode III fracture loading lasts longer. On the other hand, in studies of in-plane cracks (Ren et al. 2021; Chen et al. 2023; Zhou et al. 2023), specimens with Arrester and Divider configurations typically exhibit similar peak loads, whereas specimens with the Short-transverse configuration tend to have significantly lower peak loads compared to those with the other two configurations. However, based on the experimental results of this work, the specimens with the Arrester configuration exhibit a relatively smaller peak load for mode III fracture compared to those with the Divider configuration, with a difference of approximately 8.67%. Moreover, the peak load of the Arrester configuration specimens is very similar to that of the Short-transverse configuration specimens, with average peak loads of 2.054 kN and 2.008 kN, respectively.

The statistical distribution of the AE signals during the loading process is shown in Fig. 8. The AE signals exhibit distinct stage-dependent changes throughout the loading

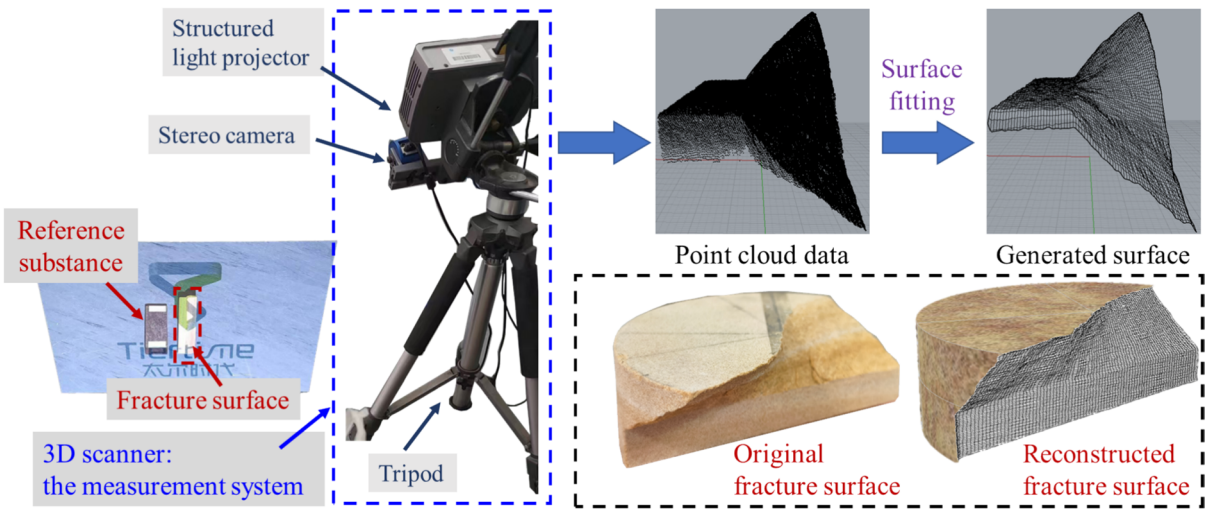

Fig. 6 Scanning and reconstruction of fracture surface

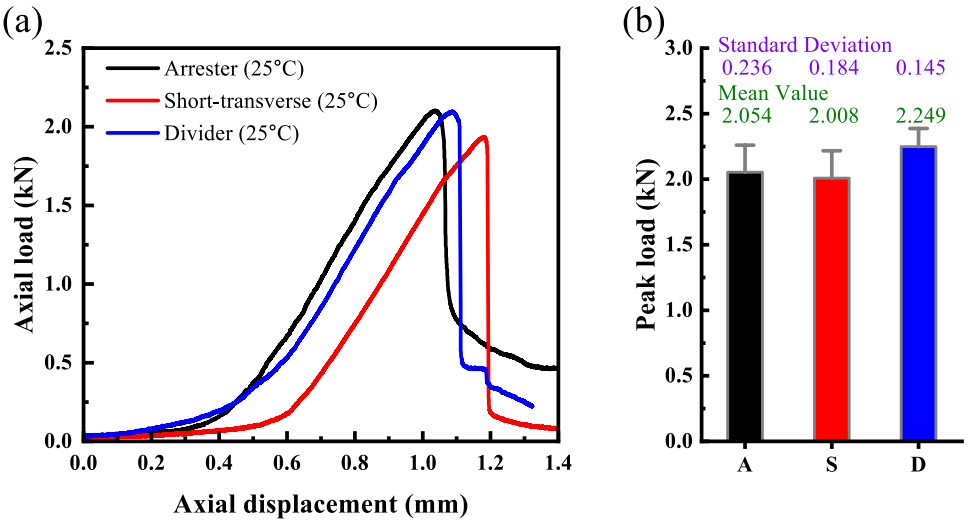

Fig. 7 **a** Typical axial load-axial position curve and **b** Peak load of ENDB sandstone specimens with different anisotropic configurations

process. Based on the amplitude characteristics of the AE signals in this work, the signals are categorized into three types: low-amplitude signals (30–50 dB), medium-amplitude signals (50–70 dB), and high-amplitude signals (70–90 dB). In the early stages of loading, only low-amplitude signals are captured, which are primarily generated by particle sliding or micro-friction induced by specimen densification. After compaction, the elastic wave release resulting from the deformation of local defects, crack propagation, and slip along contact surfaces is characterized by a higher number of low-amplitude and medium-amplitude signals. Although there is a certain increase in the cumulative AE counts, the increase is primarily caused by isolated events. As the applied load approaches its peak, AE signals become continuously active, leading to an explosive growth in cumulative AE counts. During this stage, the number of medium-amplitude signals increases significantly, and high-amplitude signals begin to appear. A similar phenomenon was observed in the studies by Cao et al. (2024) and Zheng et al. (2023b). Based on numerical simulations, they attributed the surge in medium-amplitude signals and the emergence of high-amplitude signals to the release of considerable energy during the rapid macroscopic propagation of the main crack and interfacial delamination.

To further investigate the fracture activities during the loading process, the evolution of cumulative AE counts, normalized AE energy, and loading-time cure were jointly analyzed to divide the loading process into five distinct stages, as shown in Fig. 9a: (I) Compression phase (segment OA), (II) Elastic energy storage phase (segment AB), (III) Yielding and sliding phase (segment BC), (IV) Crack initiation and propagation phase (segment CD), and (V) Macroscopic failure phase (segment DE). Among them, point C represents the moment of crack initiation (i.e., the onset of initial fracture), while point D corresponds to the peak load. During the segment CD, crack initiation and propagation occur, accompanied by a sharp increase in AE activity and a significant release of energy. It should be noted that the AE signals used in this work were normalized using a channel-summing method, which integrates the signals captured by six channels. The cumulative counts and normalized energy variations of both the individual channel signals and the superimposed signals were statistically compared, as shown in Fig. 9b and c. The results indicate that the channel signal superposition method accurately reflects the evolution of the fracture signals, effectively eliminating the noise interference from individual channels.

Energy analysis is an important tool in the study of rock fracture mechanics. By neglecting the influence of heat exchange and the kinetic energy of debris, the initial fracture energy and peak fracture energy of mode III fracture can be obtained by combining the stage division of AE signals. These energies correspond to the mechanical energy provided by the testing machine at the respective moments (Zhao et al. 2024a; Shui et al. 2024), as shown in Fig. 10. Figure 10b and c show the variations in the initial fracture energy and peak fracture energy among the three configuration specimens. The fracture energy differences for the Arrester and Short-transverse configuration specimens do not follow the same trend as the differences in peak load. In both cases, the fracture energy of the Short-transverse configuration samples is smaller than that of the Arrester configuration specimens. At the crack initiation moment, the initial fracture energy required for the Short-transverse configuration specimens is significantly lower than that for the Arrester configuration samples, with a difference of approximately 29.32% of the initial fracture energy of the Arrester configuration specimens. Both the initial and peak fracture energies of the Divider configuration specimens are higher than those of the Arrester configuration specimens, with

Table 2 Generalized mode III fracture parameters of ENDB sandstone specimens with different bedding configurations under various thermal treatment temperatures

No	Configuration	Condition	Peak load (kN)	SIF_{ini} (MPa $mm^{0.5}$)	SIF_{peak} (MPa $mm^{0.5}$)	W_i (J)	W_p (J)
1-25-1	Arrester	Unheated	2.260	0.179	0.190	0.661	0.776
1-25-2	Arrester	Unheated	1.796	0.135	0.151	0.446	0.592
1-25-3	Arrester	Unheated	2.105	0.154	0.177	0.522	0.726
1-75-1	Arrester	75 °C	1.839	0.140	0.154	0.408	0.542
1-75-2	Arrester	75 °C	2.253	0.144	0.189	0.474	0.846
1-75-3	Arrester	75 °C	2.064	0.157	0.173	0.448	0.573
1-150-1	Arrester	150 °C	1.906	0.132	0.160	0.322	0.619
1-150-2	Arrester	150 °C	2.246	0.176	0.189	0.482	0.572
1-150-3	Arrester	150 °C	1.849	0.141	0.155	0.432	0.550
1-200-1	Arrester	200 °C	1.812	0.132	0.152	0.358	0.524
1-200-2	Arrester	200 °C	1.819	0.149	0.153	0.351	0.446
1-200-3	Arrester	200 °C	2.088	0.162	0.175	0.534	0.695
1-400-1	Arrester	400 °C	1.577	0.121	0.132	0.338	0.419
1-400-2	Arrester	400 °C	1.998	0.152	0.168	0.434	0.562
1-400-3	Arrester	400 °C	1.544	0.109	0.130	0.279	0.408
1-600-1	Arrester	600 °C	0.968	0.072	0.081	0.247	0.323
1-600-2	Arrester	600 °C	1.082	0.085	0.091	0.299	0.386
1-600-3	Arrester	600 °C	1.050	0.080	0.088	0.280	0.372
2-25-1	Short-transverse	Unheated	2.217	0.139	0.176	0.451	0.768
2-25-2	Short-transverse	Unheated	1.937	0.114	0.154	0.336	0.651
2-25-3	Short-transverse	Unheated	1.871	0.126	0.149	0.363	0.563
2-75-1	Short-transverse	75 °C	1.892	0.132	0.150	0.378	0.534
2-75-2	Short-transverse	75 °C	1.834	0.097	0.146	0.255	0.527
2-75-3	Short-transverse	75 °C	2.266	0.118	0.180	0.348	0.785
2-150-1	Short-transverse	150 °C	1.947	0.117	0.155	0.329	0.563
2-150-2	Short-transverse	150 °C	1.925	0.128	0.153	0.339	0.541
2-150-3	Short-transverse	150 °C	2.042	0.101	0.162	0.269	0.573
2-200-1	Short-transverse	200 °C	1.910	0.128	0.152	0.348	0.560
2-200-2	Short-transverse	200 °C	1.791	0.109	0.142	0.254	0.449
2-200-3	Short-transverse	200 °C	1.918	0.107	0.152	0.252	0.533
2-400-1	Short-transverse	400 °C	1.723	0.106	0.137	0.300	0.478
2-400-2	Short-transverse	400 °C	1.735	0.108	0.138	0.289	0.484
2-400-3	Short-transverse	400 °C	1.609	0.104	0.128	0.252	0.417
2-600-1	Short-transverse	600 °C	1.089	0.075	0.087	0.260	0.373
2-600-2	Short-transverse	600 °C	0.921	0.060	0.073	0.173	0.271
2-600-3	Short-transverse	600 °C	0.925	0.060	0.074	0.205	0.309
3-25-1	Divider	Unheated	2.098	0.156	0.170	0.650	0.767
3-25-2	Divider	Unheated	2.262	0.147	0.184	0.670	0.837
3-25-3	Divider	Unheated	2.387	0.182	0.194	0.748	0.871
3-75-1	Divider	75 °C	2.361	0.161	0.192	0.642	0.765
3-75-2	Divider	75 °C	2.138	0.143	0.174	0.568	0.690
3-75-3	Divider	75 °C	2.226	0.146	0.181	0.534	0.664
3-150-1	Divider	150 °C	2.307	0.161	0.187	0.461	0.565
3-150-2	Divider	150 °C	1.844	0.125	0.150	0.488	0.585
3-150-3	Divider	150 °C	2.384	0.154	0.194	0.510	0.776
3-200-1	Divider	200 °C	2.026	0.143	0.165	0.412	0.607
3-200-2	Divider	200 °C	2.073	0.148	0.168	0.484	0.649
3-200-3	Divider	200 °C	2.284	0.153	0.185	0.488	0.708
3-400-1	Divider	400 °C	2.084	0.142	0.169	0.494	0.744
3-400-2	Divider	400 °C	1.777	0.24	0.144	0.390	0.562

Table 2 (continued)

No	Configuration	Condition	Peak load (kN)	SIF_{ini} (MPa $mm^{0.5}$)	SIF_{peak} (MPa $mm^{0.5}$)	W_i (J)	W_p (J)
3-400-3	Divider	400 °C	1.732	0.114	0.141	0.301	0.491
3-600-1	Divider	600 °C	1.036	0.075	0.084	0.264	0.344
3-600-2	Divider	600 °C	1.078	0.077	0.088	0.305	0.421
3-600-3	Divider	600 °C	1.051	0.077	0.085	0.295	0.399

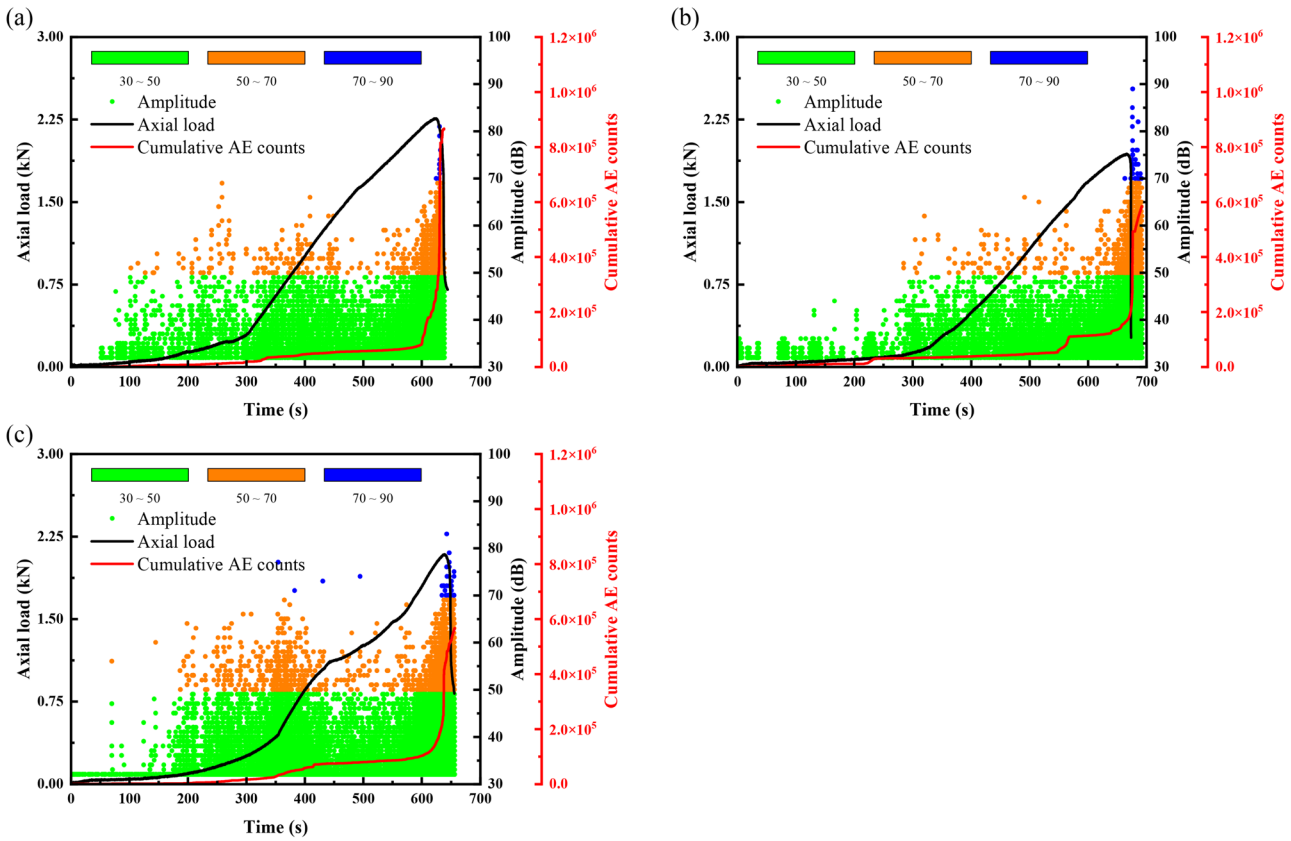

Fig. 8 Mode III fracture AE signals of ENDB sandstone specimens with different transverse isotropic configurations under loading process: **a** arrester; **b** short-transverse; **c** divider

the initial fracture energy and peak fracture energy of the Divider configuration specimens being 27.00% and 18.18% higher, respectively, than those of the Arrester configuration specimens.

In addition to fracture energy analysis, this work also uses the mode III stress intensity factors at two key moments (the initial fracture moment and the peak load moment) to quantitatively characterize the intensity of the stress field at the crack tip and the driving force for crack propagation during mode III fracture. As shown in Fig. 11a and b, the peak stress intensity factor (SIF_{peak}) was calculated using geometric factors under isotropic conditions and the geometric factors considering the transverse isotropy characteristics, respectively. From the stress intensity factor trends of the three specimen configurations, it can be seen that the stress intensity factors calculated using the geometric factors under isotropic conditions aligns well with the variation trend of the peak load for the three configurations. However, this trend does not match the variation in fracture energy. In contrast, the stress intensity factor trend calculated using the geometric factors that account for the transverse isotropy characteristics shows a weaker correlation with the peak load variation but a stronger consistency with the trend of fracture energy.

On the one hand, the anisotropy of the material in the crack tip region and the non-coplanarity of the applied load and the prefabricated notch led to a non-linear relationship between the peak load and the stress field. Therefore, the

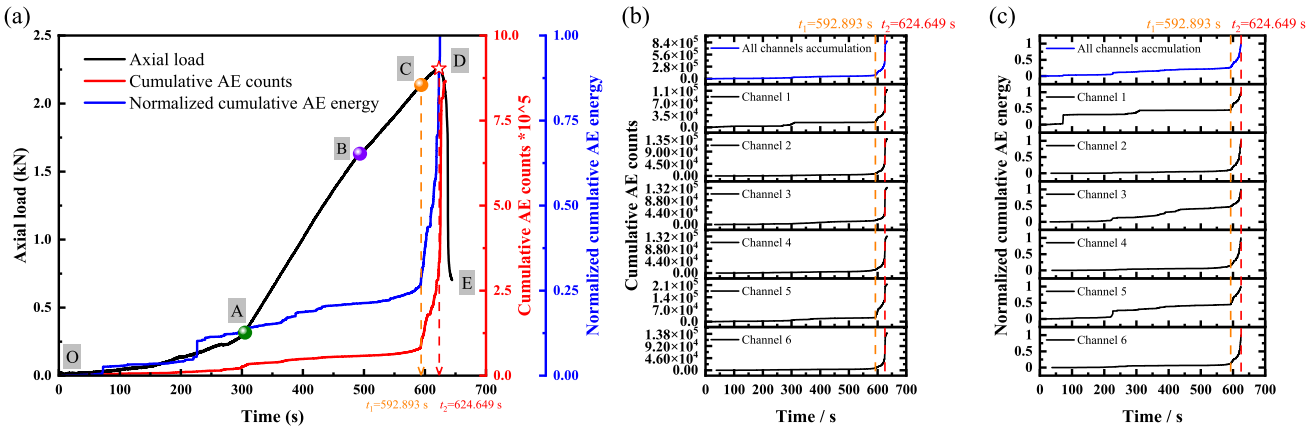

Fig. 9 **a** Segmentation of loading process based on AE signals; reliability verification of channel superposition signal characterization: **b** cumulative AE counts and **c** normalized cumulative AE energy

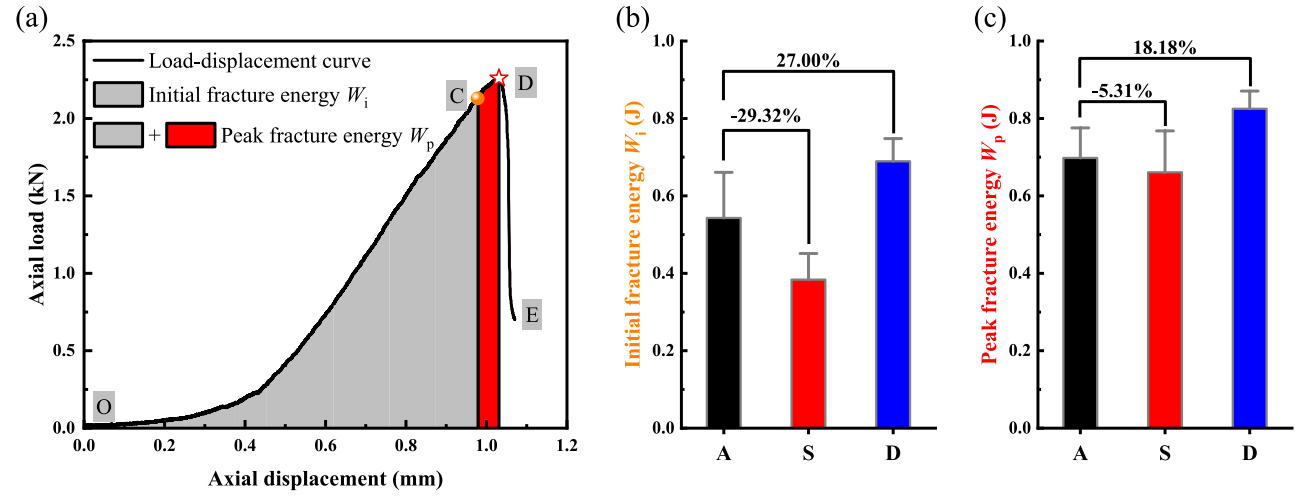

Fig. 10 Fracture energy of transversely isotropic sandstone ENDB specimen: **a** schematic diagram of energy calculation; **b** initial fracture energy; **c** peak fracture energy

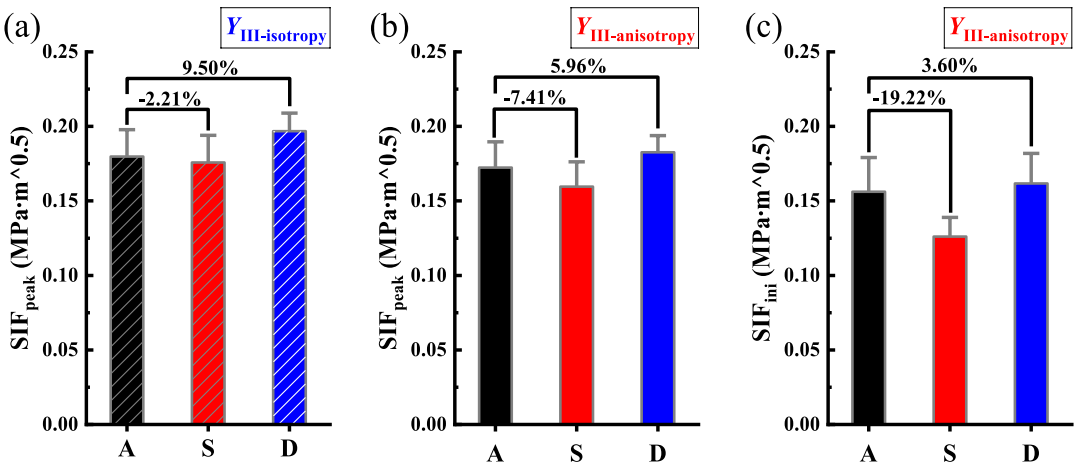

Fig. 11 Characteristic stress intensity factors: **a** peak stress intensity factors calculated by $Y_{\text{III-isotropy}}$; **b** peak stress intensity factors calculated by $Y_{\text{III-anisotropy}}$; **c** initial stress intensity factor calculated by $Y_{\text{III-anisotropy}}$

peak load merely reflects the magnitude of the externally applied load, rather than directly characterizing the stress intensity at the crack tip. On the other hand, the stress concentration at the crack tip is redistributed due to the anisotropic nature of the material (Suo et al. 2020), resulting in an inconsistent relationship between the peak load and the driving force at the crack tip. Consequently, the peak stress intensity factor of transverse isotropic ENDB sandstone specimens should exhibit a non-direct correlation with the peak load. In addition, the peak load is a global loading characteristic and cannot accurately reflect the local mechanical behavior at the crack tip. In contrast, the fracture energy and stress intensity factor can reflect the local stress field and energy dissipation characteristics at the crack tip, and are related to the directional shear modulus of anisotropy materials. In summary, geometry factors that account for transverse isotropy offer a more accurate representation of the local stress field intensity characteristics at the crack tip of the specimen.

The mode III peak stress intensity factor and initial stress intensity factors for the three specimen configurations, calculated using geometry factors that account for the transverse isotropy characteristics of the specimen, are shown in Fig. 11b and c. For both types of stress intensity factors, the descending order is: Divider configuration > Arrester configuration > Short-transverse configuration. Specifically, for the peak stress intensity factor, the Short-transverse configuration is 7.41% lower than the Arrester configuration, while the Divider configuration is 5.96% higher than the Arrester configuration. For the initial stress intensity factor, the Short-transverse configuration is 19.22% lower than the Arrester configuration, and the Divider configuration is 3.6% higher than the Arrester configuration. Combining these results with the fracture energy analysis of the three configurations, it can be observed that when the weak plane is in the Short-transverse configuration relative to the bedding, crack initiation tends to occur earlier, even though the peak stress intensity factor of the Short-transverse configuration is not significantly lower than that of the other two configurations. Therefore, in practical engineering applications involving safety and stability assessment, attention should not only be given to whether the stress intensity factor exceeds the peak stress intensity factor but also to its relation to the initial stress intensity factor.

3.2 Influence of Thermal Effect on Mode III Fracture Behavior of Transversely Isotropic Sandstone

Figure 12 shows the typical axial load-axial displacement curves of the three configurations of specimens undergoing generalized mode III fracture after heat treatment at different temperatures. The post-peak behavior is annotated with red and black arrows to indicate gradual and rapid post-peak load drops, respectively. The thermal effect has a varying impact on the load–displacement response relationship for different specimen configurations. For the Arrester configuration specimens, unlike the Divider configuration specimens (which exhibits gradual post-peak load decline only when the temperature rises to 200–400 °C), the load decreases gradually in the post-peak stage at all tested temperatures. This phenomenon cannot be solely attributed to the ductile behavior of the material; it may also be caused by interface sliding (Cao et al. 2024), especially in specimens that were either untreated or subjected to relatively low heat

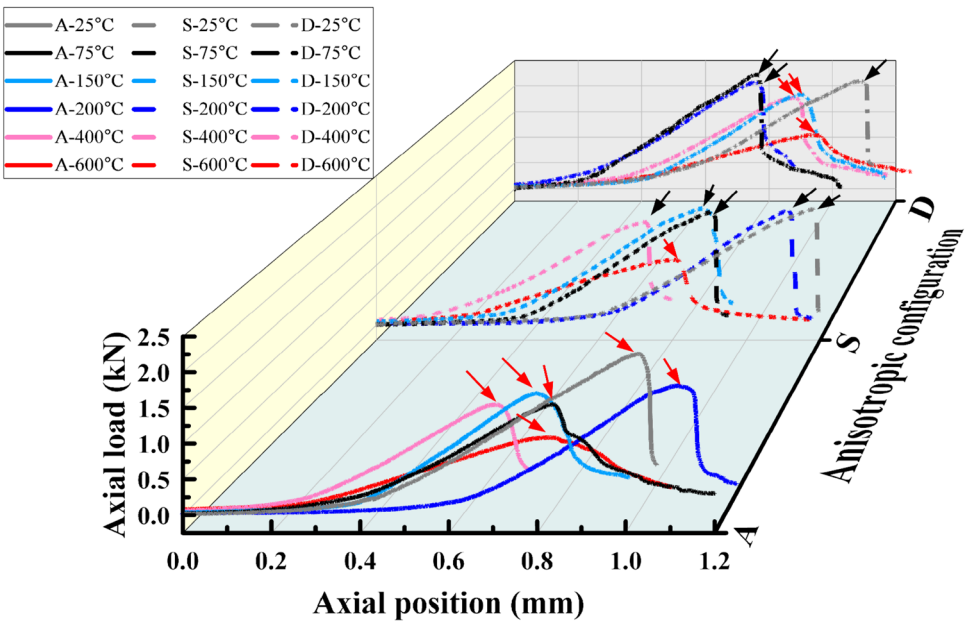

Fig. 12 Typic axial load-axial displacement curves of specimens after heat treatment at different temperatures

treatment temperatures. For the Short-transverse configuration specimens, a ductile-sliding post-peak response (Cao et al. 2024) is only when the heat treatment temperature reaches 600 °C. Although specimens of this configuration treated below 600 °C (or untreated) also exhibit a tendency for interfacial slip as cracks propagate across bedding interfaces, the relative motion involved differs from that in ductile-sliding behavior. Specifically, the former type of slip tends to promote failure, whereas the latter reflects more progressive deformation. This distinction is further analyzed in Sect. 4.2.

Figure 13 shows the peak load and the corresponding displacement of the three configurations of specimens after heat treatment at different temperatures during generalized mode III fracture. Under the influence of thermal effects, the peak load of all three configurations decreases as the heat treatment temperature increases. Moreover, as the temperature rises, the rate of decrease in peak load becomes more pronounced. Specifically, the load difference between specimens treated at 600 °C and 400 °C is greater than that between 400 °C and 200 °C, which is in turn greater than that between 200 °C and the untreated specimens. The displacement at peak load shows a weak correlation with the bedding configuration, but it is significantly affected by thermal treatment. In the range of 25–150 °C, the displacement at peak load shows a decreasing trend; at 200 °C, it increases. When the temperature reaches 400 °C, the displacement decreases again, and at 600 °C, it no longer decreases significantly, showing only a slight difference compared to that at 400 °C. Based on the variation patterns of peak load and displacement at peak load after different thermal treatments, the heat treatment temperatures can be divided into three intervals: low-temperature range (25–200 °C), medium-temperature range (200–400 °C), and high-temperature range (400–600 °C).

The thermal effects influence not only the overall load-bearing capacity of the specimens but also the stress field intensity at the crack tip. As shown in Fig. 14a and b, the initial stress intensity factor and peak stress intensity factor of the three specimen configurations under generalized mode III fracture gradually decrease with increasing thermal treatment temperature. The rate of decrease follows the order: the high-temperature range > medium-temperature range > low-temperature range. In the low-temperature range (25–200 °C), the initial stress intensity factor shows the most significant reduction at 75 °C, and then tends to stabilize. As for the peak stress intensity factor, it shows the most significant reduction at 150 °C, while the peak stress intensity factor of the specimens treated at 75 °C is nearly the same as that of the untreated specimens. Generally, thermal treatment below 150 °C primarily causes the release of free water and bound water (Wong et al. 2020). Therefore, it can be inferred that the initial stress intensity factor is more sensitive to the escape of free water. At 75 °C, the escape of free water from the liquid to vapor phase induces a redistribution of local thermal stresses, but is insufficient to initiate significant thermal cracking. However, at 150 °C, bound water begins to escape as well, resulting in the initiation of microcracks due to thermal expansion, which leads to a decrease in peak stress intensity factor. When the treatment temperature reaches 400 °C, structural changes in clay minerals occur (e.g., oxidation of iron oxides, Ersoy et al. 2021), and differential thermal expansion among minerals intensifies intergranular thermal stress (Yang et al. 2024), accelerating the development of thermal caracks and increasing porosity. At 600 °C, in addition to the physical transformation

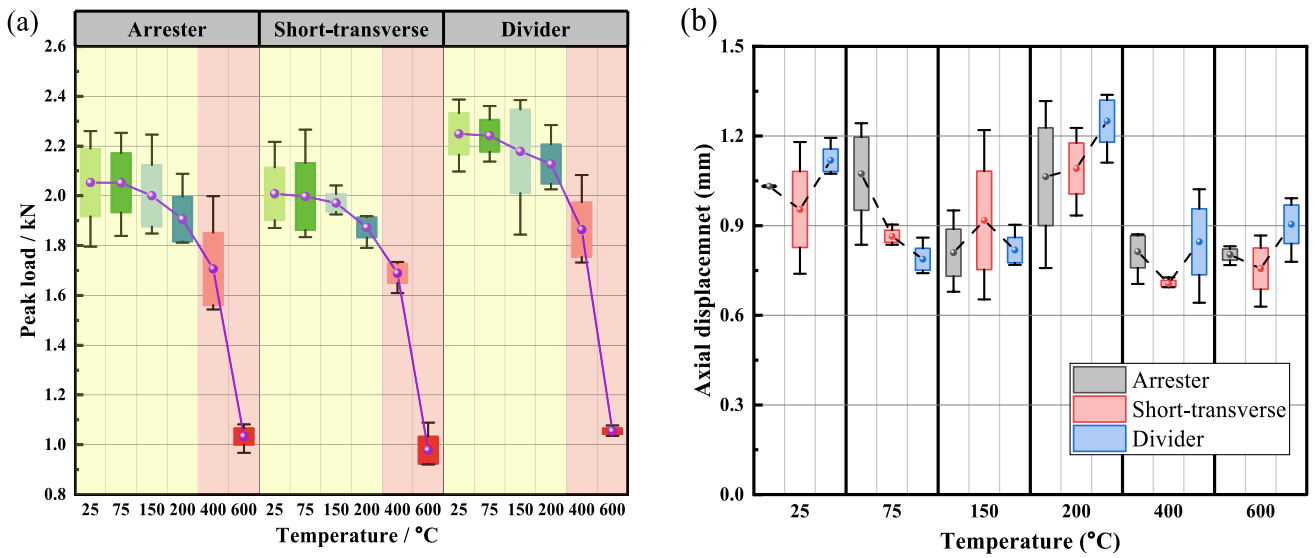

Fig. 13 The peak axial load and displacement at the peak load with temperature change

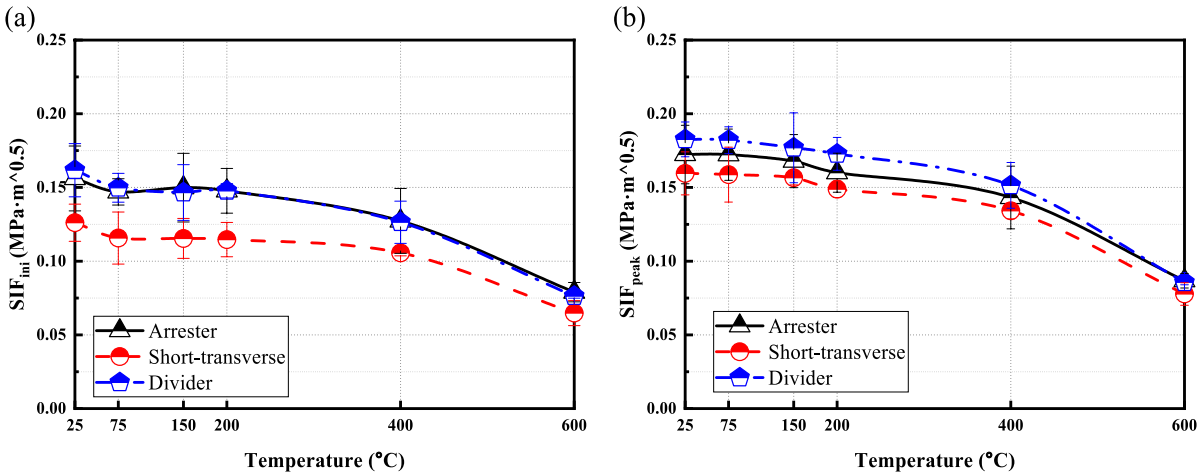

Fig. 14 Influence of thermal effect on characteristic stress intensity factors of mode III fracture of transverse isotropic sandstone: **a** Initial stress intensity factor; **b** peak stress intensity factor

of quartz (phase transition, Shi et al. 2024; Su et al. 2022), chemical processes such as the decomposition of calcite and lattice collapse of clay minerals may occur, which further promote the formation of through-going cracks and the enlargement of pore spaces (Shen et al. 2020).

The thermal effect exhibits a consistent influence on the variation trend of characteristic stress intensity factors across different bedding configurations. However, it alters the extent to which bedding configuration affects the characteristic stress intensity factors. For the peak stress intensity factor, in both the low-temperature and medium-temperature ranges, the order of values at the same thermal treatment temperature is Divider configuration > Arrester configuration > Short-transverse configuration. The difference in peak stress intensity factor among the three configurations gradually diminishes as the treatment temperature increases, indicating that thermal effects reduce the sensitivity of peak stress intensity factor to bedding configuration. Notably, at 600 °C, the peak intensity factors of Divider and Arrester configurations are nearly identical. For the initial stress intensity factor, the influence of thermal effects on the Divider and Arrester configuration specimens is more significant, and the initial stress intensity factors of both specimens after heat treatment become nearly equal.

By statistically analyzing the mode III initial and peak stress intensity factors of the three configurations specimens after different level of thermal treatment (Fig. 15), it is found that the thermally treated transversely isotropic sandstone specimens still exhibit a significant linear relationship between the initial and peak stress intensity factors. Fitting the linear relationship for each configuration shows that the proportionality coefficient (i.e., the slope of the fitted line) follows the order: Arrester > Divider > Short-transverse. This indicates that among the three configurations,

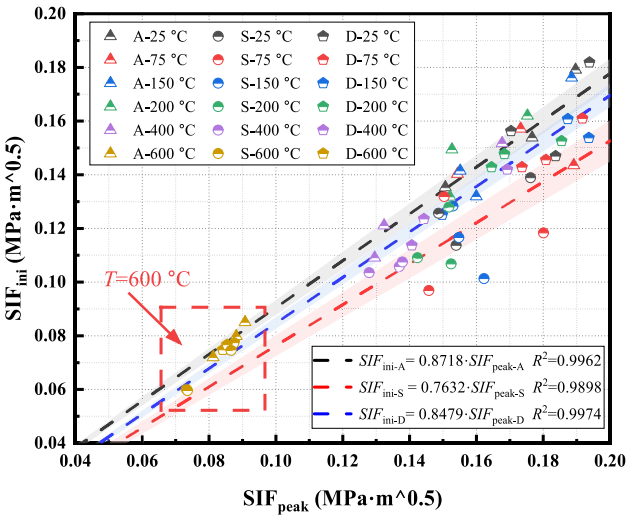

Fig. 15 Correlation between the initial stress intensity factor and peak stress intensity factor

the initial stress intensity factor of the Arrester specimens is the closet to their peak stress intensity factor. Although cracks in Short-transverse specimens tend to initiate more easily compared to the other two configurations, their further crack propagation requires a relatively greater increase in the crack-tip stress field intensity. From the perspective of fracture energy, as shown in Fig. 16a and b, the initial fracture energy of the Short-transverse specimens is significantly lower than the fracture energy at the peak load point. For all three configurations, both the initial and peak fracture energies decrease with increasing thermal treatment temperature. Moreover, the magnitudes of these reductions differ across temperature ranges. The greatest reductions in both initial

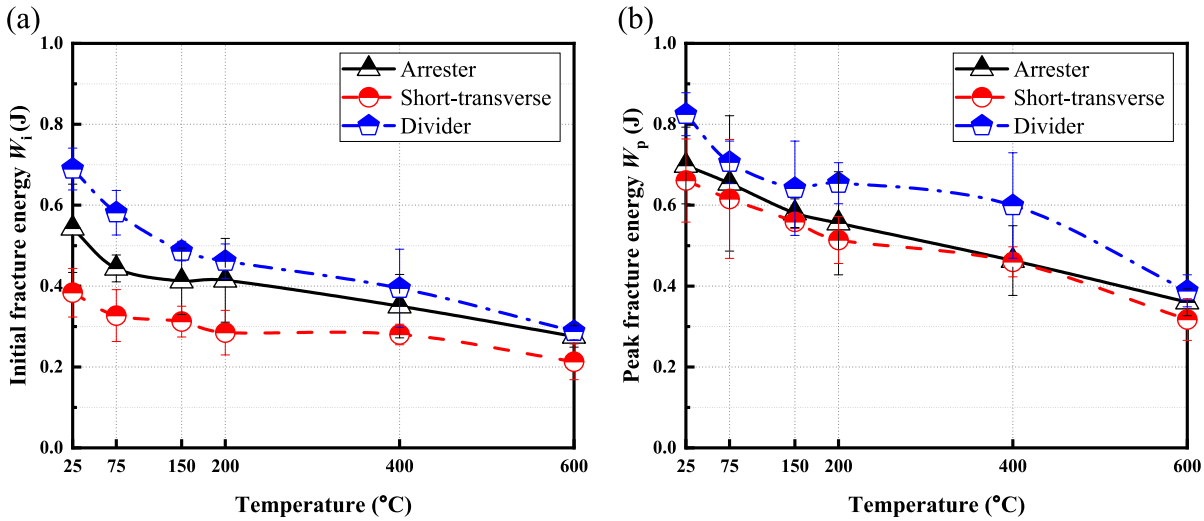

Fig. 16 Relationship between key fracture energy and heat treatment temperature: **a** initial fracture energy; **b** peak fracture energy

and peak fracture energy occur in the high-temperature range, followed by the medium-temperature range.

Previous studies have shown that the number and type of cracks can be further quantified based on AE counts. The *RA* value (Rise time/Amplitude) and *AF* value (Ring count/Duration time, average frequency) of the AE signals during the mode III fracture process of the three configuration specimens at different temperatures are shown in Fig. 17. It is generally accepted that tensile cracks occur when the tensile stress exceeds the tensile bonding strength at the interface, releasing elastic waves characterized by low *RA* values and high *AF* values. While shear cracks occur when the shear stress exceeds the shear bonding strength, releasing elastic waves with high *RA* values and low *AF* values.

Currently, there is no universally accepted standard for classifying cracks based on RA and AF parameters. Two main approaches have been proposed to determine classification boundaries: (i) Statistical classification models, such as threshold segmentation and principal component analysis. Some studies have adopted a threshold of $RA/AF = 1$ (with units of kHz, μs/dB, or μs/V) for classification (Zhuang and Zang 2021), while others have established threshold values based on direct shear or splitting tests (Du et al. 2020). (ii) Machine learning classification algorithms, including supervised learning approaches such as support vector machines, decision trees/random forests, and neural networks, as well as unsupervised learning approaches such as clustering analysis (Jiang et al. 2024). Among these methods, K-means clustering and threshold segmentation have been widely used due to their advantage of not requiring large datasets to achieve reliable classification (Liu et al. 2024; Jiang et al. 2025). However, since K-means clustering is based on Euclidean distance, it performs poorly when the data exhibit significant feature biases (as shown in Fig. 17a, where the signal distribution increasingly skews toward high *RA* values and low *AF* values with rising temperature). In cases where tensile and shear cracks form non-circular distributions on the *RA*-*AF* plane, K-means clustering may fail to distinguish them accurately. Threshold segmentation methods depend on the material properties and testing conditions and therefore lack complete universality. Based on these considerations, this work ultimately adopts $RA/AF = 1$ as the classification threshold for distinguishing crack types.

It can be observed that (in Fig. 17), among the untreated three configuration specimens, the Arrester configuration specimens have a higher proportion of tensile cracks compared to the other two configurations, while the Short-transverse configuration specimens exhibit the highest proportion of shear cracks. As the heat treatment temperature increases, the number of activated cracks induced by thermal effects during loading increases, and the proportion of tensile cracks increases to varying extents.

4 Discussion

4.1 Morphological Characteristics of Fracture Surface

The fracture surface morphology is also an important tool for reconstructing the crack initiation and propagation processes (Shi et al. 2023; Zhao et al. 2024a). In particular, the crack initiation angle and final failure angle are often used in fracture mechanics studies to determine the potential crack failure path and the direction of principal stress failure (Liu et al. 2024). For the ENDB specimens, the out-of-plane crack extension and the curved surface morphology on the specimen's outer side pose challenges

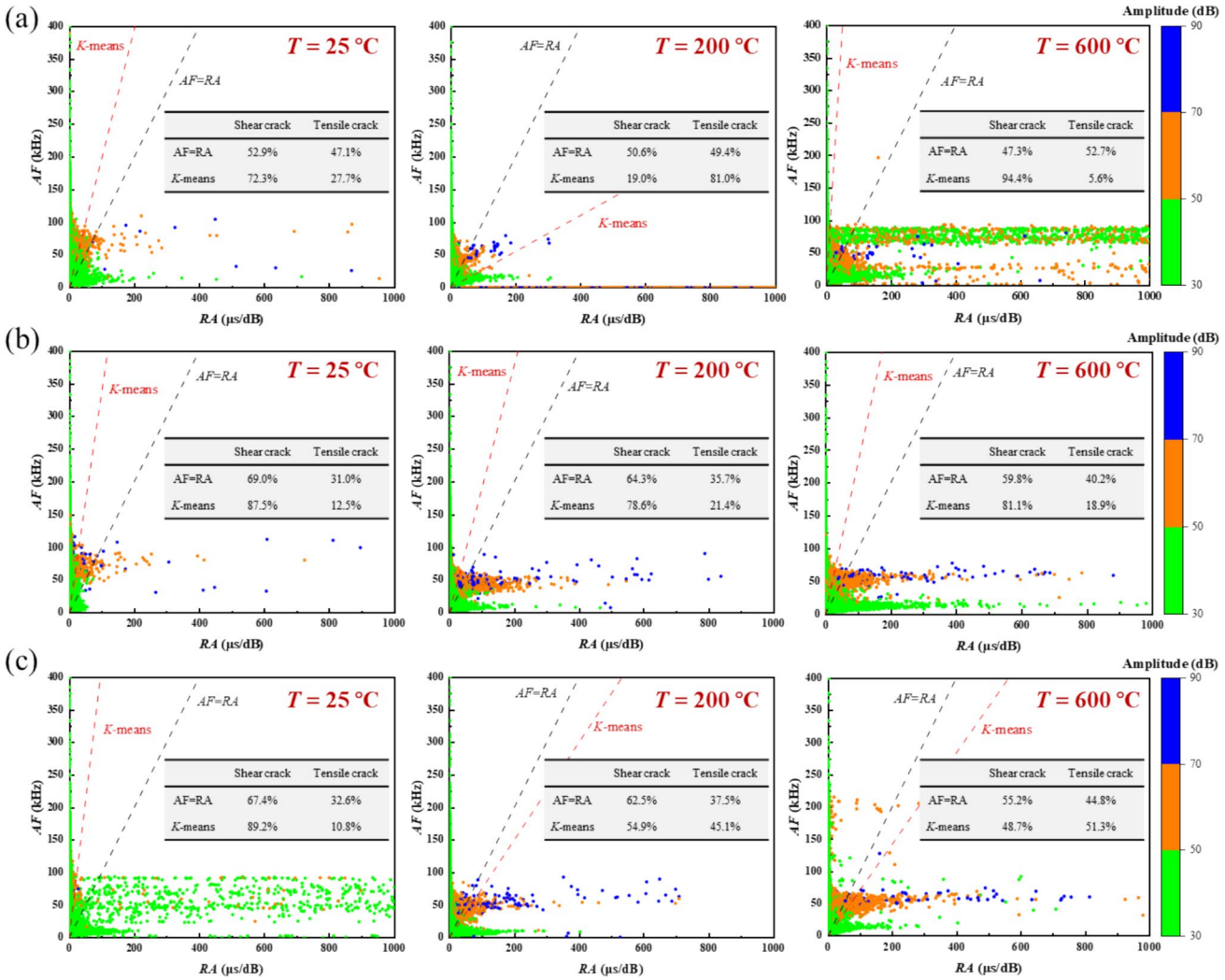

Fig. 17 The proportion of crack classification of specimens with different configurations after heat treatment: **a** arrester; **b** short-transverse; **c** divider

in measuring the angles. This work used 3D scanning technology to accurately reconstruct the morphological features of the failed specimens, as shown in Fig. 6. Based on the reconstructed numerical model, the specimen's curved surface was unfolded along the prefabricated notch to obtain the crack trajectory on the surface, as shown in Fig. 18a. Statistical analysis of the crack initiation angle and final failure angle, as shown in Fig. 18b, reveals that the bedding perpendicular to the prefabricated notch plane results in the Arrester configuration specimens having the smallest crack initiation and final failure angles among the three configurations, while the bedding parallel to the prefabricated notch plane leads to the Short-transverse configuration specimens having the largest crack initiation and final failure angles.

To quantitatively evaluate the fracture surface morphology characteristics of mode III fracture, the fracture surface within the region $-2/3 \le X/R \le 2/3$ is selected as the area of interest (in Fig. 19a), based on the K_I, K_{II}, K_{III}, and T-stress distribution of the ENDB specimens (Bahmani et al. 2021). The box-counting fractal dimension method is employed, where cubic boxes with side length δ are used to fill the fracture surface on the XOY plane, and the number of boxes $N(\delta)$ required is counted. The side length δ of the boxes is progressively reduced, and the slope of the linear fit of $\ln N(\delta) \sim \ln \delta$ is obtained using the least squares method according to Eq. (4), yielding the fractal dimension (D_f)of the fracture surface (Shi et al. 2023; Zhao et al. 2024a).

$$D_f = -\lim_{\delta \to 0} \frac{\ln N(\delta)}{\ln \delta} \tag{4}$$

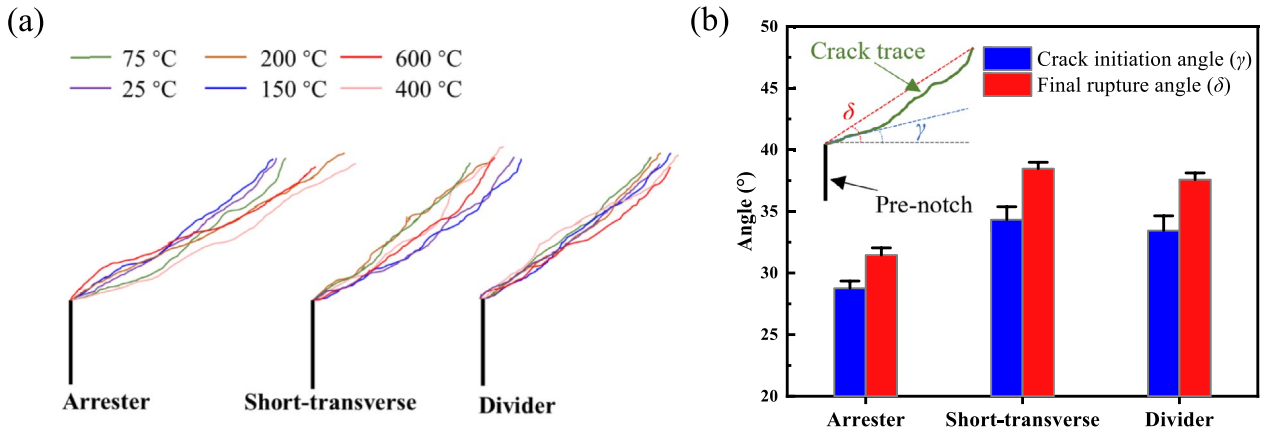

Fig. 18 Cracks on the cylindrical surface: **a** trace; **b** fracture angle

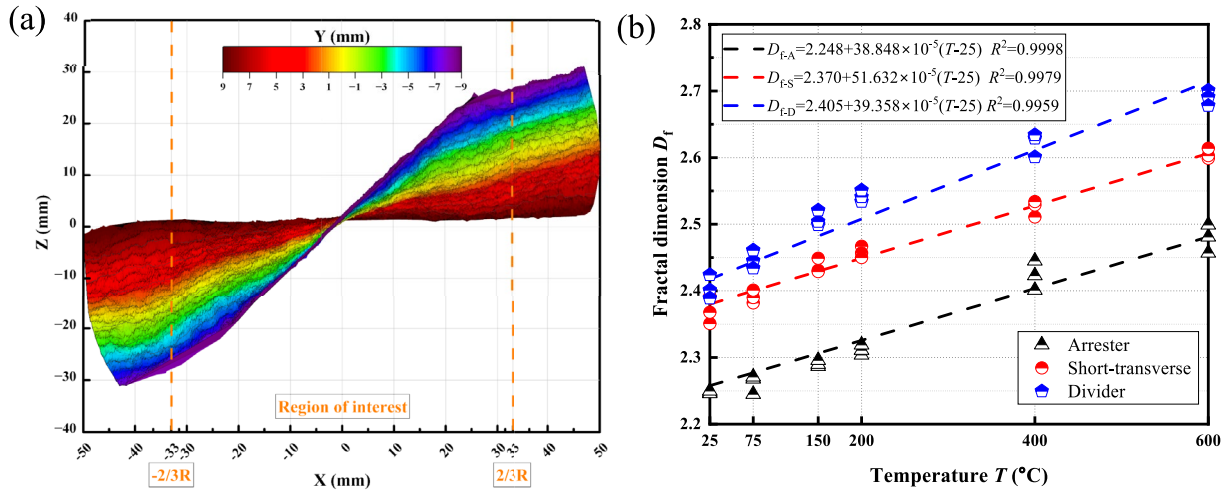

Fig. 19 **a** ROI of fracture surface; **b** fractal dimension of the fracture surface

The relationship between the D_f of the fracture surface and the heat treatment temperature for the three configuration specimens is shown in Fig. 19b. The D_f of the fracture surface for different configuration specimens increases with rising thermal temperature, exhibiting a clear linear relationship. This indicated that specimens subjected to higher temperatures develop fracture surfaces that are more complex, rougher, and more irregular. Thermally induced cracks interfere with the original propagation path of mode III fracture, leading to phenomena such as crack branching, deflection, and segmentation, all of which increase the irregularity of the fracture surface (Shi et al. 2023). Microstructural changes, mineral phase transitions, pore structure alterations, and increased complexity of crack propagation caused by thermal effects may all contribute to the higher complexity observed in the fracture surface (Su et al. 2022; Yin et al. 2021). The higher the treatment temperature, the more significant the thermal effects, resulting in a higher fractal dimension of the fracture surface.

4.2 Mechanism of Crack Propagation

To further investigate the mode III crack propagation mechanism of thermally treated transversely isotropic sandstone, the fracture signal source localization map during loading was obtained using the TDOA method, as shown in Fig. 20 (due to space limitations, only the Arrester configuration specimen is presented as an example). Compared with the unheated specimen, the thermally treated specimen exhibits a significantly larger number of localized fracture signals. This increase is attributed to the pre-damage effects induced by thermal treatment (Shi et al. 2023; 2024), such as thermal stress and mineral phase transitions, which make the rock more susceptible to triggering chain micro-crack

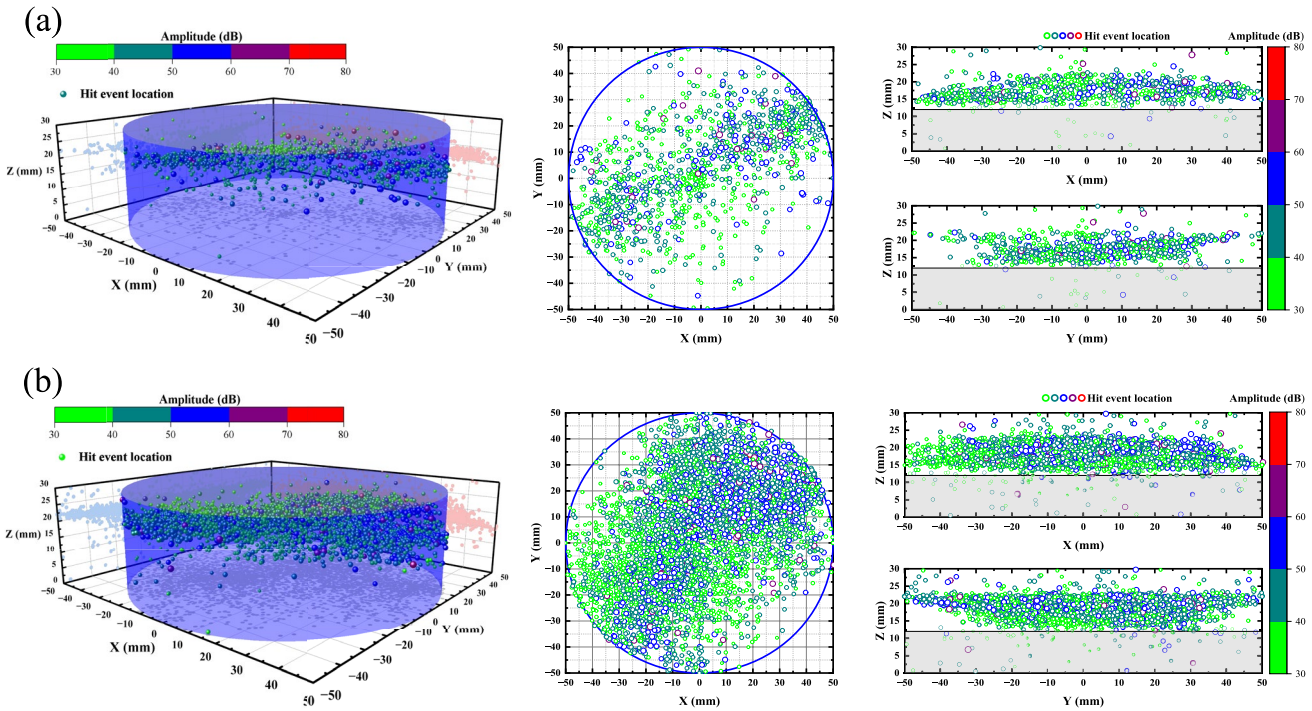

Fig. 20 The 3D location and 2D projections of the fracture signal in Arrester configuration specimens: **a** 25 °C; **b** 600 °C

during loading. In terms of spatial distribution, both thermally treated and unheated specimens show that medium-amplitude and high-amplitude signals are primarily concentrated in the vicinity of the prefabricated notch. In contrast, low-amplitude signals, likely associated with pore closure and particle friction (Du et al. 2020; Xia et al. 2022), are distributed more extensively and are not confined to the vicinity of the prefabricated notch.

Based on the spatial density characteristics of fracture signals (Fig. 21), the thermally treated specimens exhibit a broader distribution range of concentrated signal zones (bright bands) compared to the untreated specimens. Furthermore, the XZ and YZ projections reveal that the signal concentration zones in the thermally treated specimens display a distinct horizontal distribution pattern. Considering the bedding structure of the specimens, it can be inferred that thermal treatment leads to deterioration at the interfaces between the horizontal bedding planes and the surrounding matrix, making these regions more prone to fracture during subsequent loading. The presence of bedding not only causes fracture to concentrate along the bedding-matrix interfaces but also contributes to deviations in the fracture path. As shown in Fig. 22, the spatial relationship between the AE source localization data and the reconstructed fracture surface reveals that the AE signals do not propagate along an idealized fracture surface (represented by the orange surface, Aliha et al. 2019). Instead, influenced by the bedding, the crack propagates in a twisted trajectory around the specimen's central axial, from the prefabricated notch tip (purple surface) toward the loading end. Combined with the spatial distribution characteristics of AE signals with different amplitudes (Fig. 20), the crack propagation process can be inferred as follows: loading alter the internal stress field, causing a rapid increase in stress intensity at the prefabricated notch tip. Pre-existing pores and micro-defects undergo closure, sliding, and dislocation (Du et al. 2020; Xia et al. 2022), releasing low-energy stress waves (low-amplitude signals) over a broad region with the specimen. Once the crack initiation threshold is reached, higher-energy stress waves (corresponding to medium-amplitude and higher-amplitude signals) are released in a concentrated manner along the developing fracture surface. As the crack twists upward during propagation, it encounters horizontal bedding planes and shows a tendency to deviate laterally, as illustrated in Fig. 23a. This interaction suppresses upward crack propagation and facilitates horizontal extension (Cao et al. 2024; Liu et al. 2023). Along the bedding planes, grains are subjected to shear forces, leading to dislocation and intergranular slip. Consequently, banded concentrations of medium-amplitude AE signals are released along the horizontal bedding interfaces.

As demonstrated above, horizontal bedding significantly influences crack initiation and propagation. To further investigate the effect of different bedding configurations on crack development, schematic diagrams

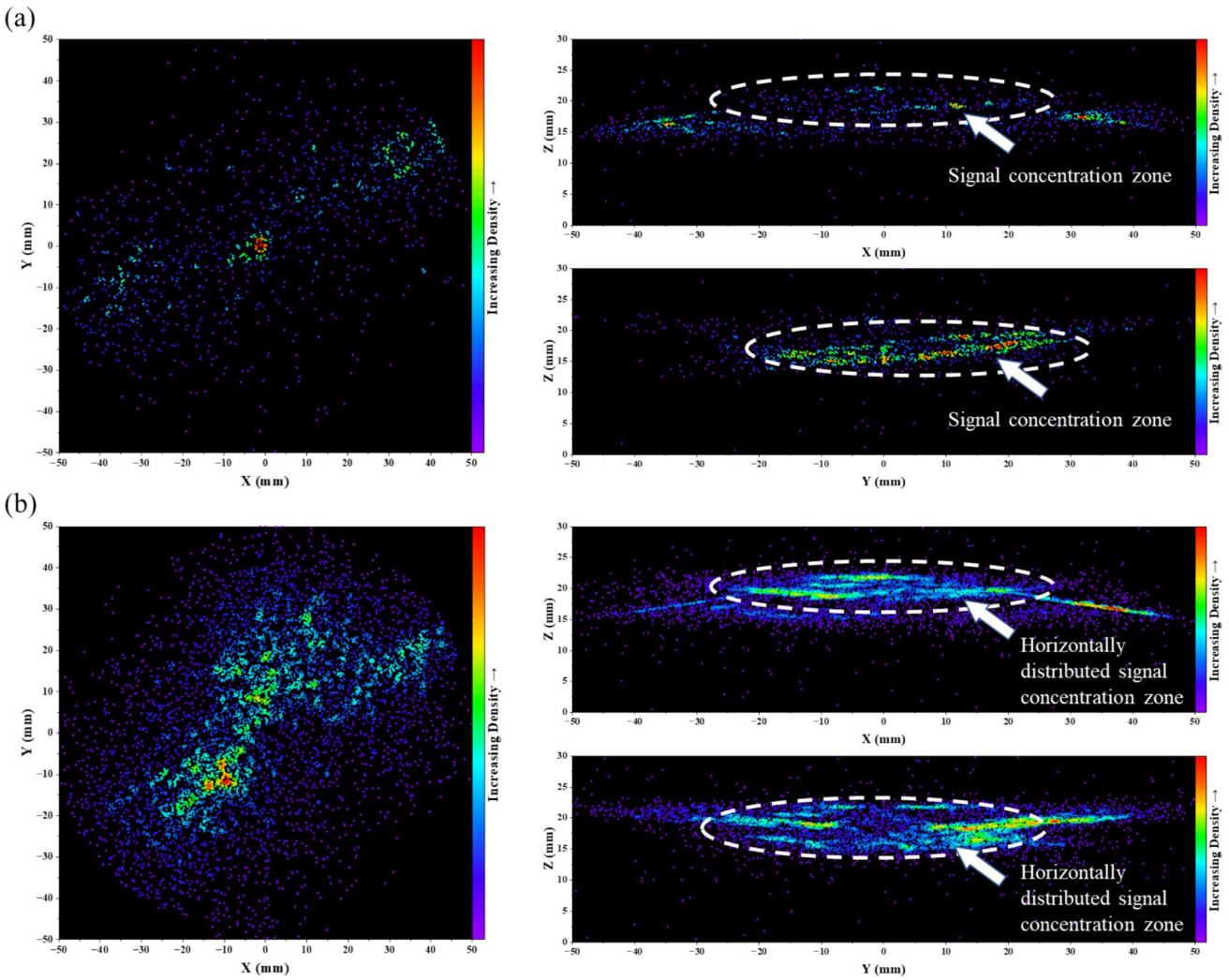

Fig. 21 Density cloud maps of the fracture signal in arrester configuration specimens: **a** 25 °C; **b** 600 °C

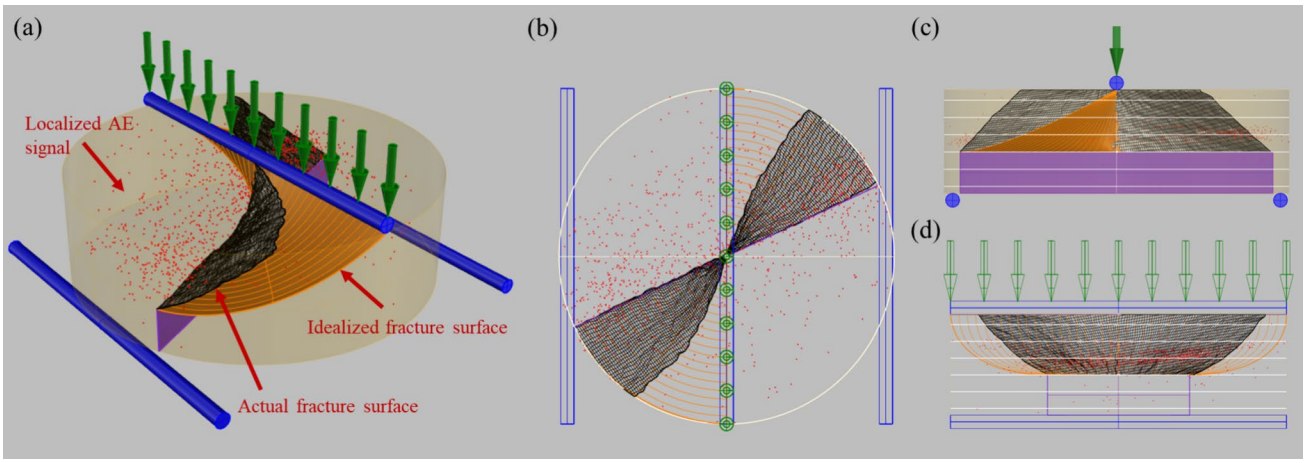

Fig. 22 The relative spatial relationship between the fracture plane and the fracture signal: **a** 3D view; **b** Top view; **c** front view; **d** side view

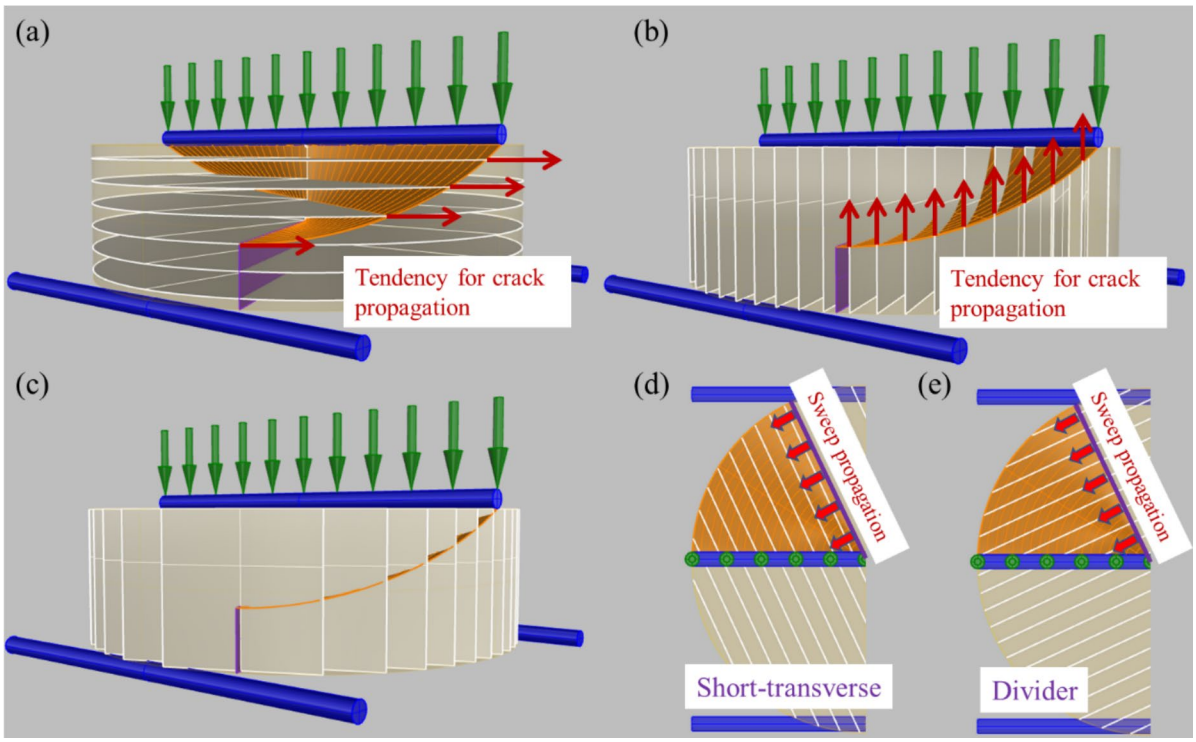

Fig. 23 Schematic illustration of crack propagation trends at bedding interfaces under different bedding configurations: **a** arrester; **b** short-transverse; **c** divider; **d** top view of the transverse; **e** top view of the divider

illustrating the spatial relationship between bedding planes and the idealized fracture surface in the three configuration specimens are presented in Fig. 23 a-c. Based on the spatial orientation of the idealized fracture surface relative to the bedding, the probable crack propagation trends can be inferred, as indicated by the red arrows in the figures. The cracks, which originally trend to propagation along the idealized fracture surface, exhibit different propagation tendencies under the influence of bedding in the three configurations. In the Arrester configuration, the bedding promotes horizontal crack propagation. In contrast, in the Short-transverse configuration, the bedding favors vertical crack propagation. As a result, both configurations require relatively lower fracture energy for crack initiation and eventual failure. Although the Divider configuration also contains vertically oriented bedding planes, the crack front extends in a spiraling upward trajectory centered around the cylindrical axis of the specimen and inclined toward the loading direction, as shown in Fig. 23 e and f. Therefore, the bedding in the Short-transverse configuration facilitates crack propagation, while in the Divider configuration it does not offer the same advantage.

5 Conclusions

In this work, ENDB transverse isotropic sandstone specimens with three different bedding configurations were subjected to varying degrees of heat treatment, followed by generalized pure mode III fracture loading of the heat-treated specimens. Based on AE and 3D scanning technologies, the influence of thermal effects on the transverse isotropy of mode III fracture behavior was discussed. The main conclusions are as follows:

(1) The spatial relationship between the bedding and the prefabricated notch directly affects the mechanical and fracture characteristics of mode III fracture, such as peak load, stress intensity factor, and fracture energy. Specifically, the Short-transverse configuration specimens exhibit lower peak loads (12.00% lower than the Divider configuration), lower fracture energy (initial and peak fracture energies are 56.32% and 23.49% lower than the Divider configuration, respectively), and lower stress intensity factors (the initial stress intensity factor and peak stress intensity factor are 22.82% and 13.37% lower than the Divider configuration, respectively), making them more prone to crack initiation.
(2) Thermal effects also influence mode III fracture behavior, with high-temperature heat treatment reducing the

effect of the bedding configuration. The correlation between the displacement at peak load and the spatial relationship of the bedding and prefabricated notch is weak, while the effect of thermal treatment on the displacement at peak load is more pronounced. Peak load decreases with increasing heat treatment temperature, and this decrease becomes more pronounced as the temperature rises. With increasing heat treatment temperature, both stress intensity factor and fracture energy gradually decrease. The rate of decrease is fastest in the high-temperature range (400–600 °C), followed by the medium-temperature range (200–400 °C), and slowest in the low-temperature range (25–200 °C).

(3) The fracture surface morphology characteristics of transverse isotropic sandstone mode III fracture are significantly affected by thermal effects. The fractal dimension of the fracture surface increases with rising heat treatment temperature, showing a linear relationship. The cracks induced by thermal effects interfere with the original propagation paths of mode III cracks, with phenomena such as crossing, splitting, and jumping increasing the irregularity of the fracture surface. The higher the temperature, the more pronounced the effect of thermal effects, leading to a higher fractal dimension of the fracture surface.

(4) The medium-amplitude and high-amplitude fracture signals are important indicators of crack initiation and propagation. In terms of time, they occur in concentrated continuous events during the crack initiation and propagation stage and the macroscopic failure stage after crack initiation. Spatially, the medium-amplitude and high-amplitude signals are mainly concentrated near the prefabricated notch. In contrast, low-amplitude signals caused by pore closure and particle friction are widely distributed throughout the entire time period and range.

Author Contributions All authors contributed to the study conception and design. Xiaofeng Qin: Conceptualization, Writing-Original Draft, Methodology, Project administration, Investigation, Formal analysis, Visualization and Data Curation. Haijian Su: Conceptualization, Writing-Review & Editing, Methodology, Project administration and Funding acquisition. Liyuan Yu: Methodology, Resources, Supervision and Funding acquisition. Thi Nhan Pham: Investigation, Resources and Data Curation. Enzhuo Zhao: Data Curation and Validation. Menglong Zhang: Data Curation and Validation. All authors read and approved the final manuscript.

Funding This study is financed by the National Natural Science Foundation of China (Nos. 52274100 and U24B2040).

Data Availability All data used to support the findings of this work are included within the article, and there are not any restrictions on data access.

Declarations

Conflict of interest The authors declare that they have no competing interests.

References

Ahmadi M, Shafabakhsh GA, Di Mascio P et al (2021) Failure behavior of functionally graded roller compacted concrete pavement under mode I and III fracture. Constr Build Mater 307:124942. https://doi.org/10.1016/j.conbuildmat.2021.124942

Aliha MRM, Mousavi SS, Bahmani A et al (2019) Crack initiation angles and propagation paths in polyurethane foams under mixed modes I/II and I/III loading. Ther Appl Fract Mech 101:152–161. https://doi.org/10.1016/j.tafmec.2019.02.016

Aliha MRM, Kouchaki HG, Haghighatpour PJ (2023) Designing a simple and suitable laboratory test specimen for investigating the general mixed mode I/II/III fracture problem. Mater des 236:112477. https://doi.org/10.1016/j.matdes.2023.112477

Alneasan M, Alzoubi AK, Behnia M et al (2022) Experimental observations on the effect of thermal treatment on the crack speed and mode I and II fracture toughness in brittle and ductile rocks. Theor Appl Fract Mech 121:103525. https://doi.org/10.1016/j.tafmec.2022.103525

Bahmani A, Farahmand F, Janbaz MR et al (2021) On the comparison of two mixed-mode I + III fracture test specimens. Eng Fract Mech 241:107434. https://doi.org/10.1016/j.engfracmech.2020.107434

Barton N, Quadros E (2015) Anisotropy is everywhere, to see, to measure, and to model. Rock Mech Rock Eng 48:1323–1339. https://doi.org/10.1007/s00603-014-0632-7

Cao RH, Yao RB, Dai H et al (2024) Fracture behaviour of transversely isotropic rocks under pure mode III fracture: experiment and numerical simulation. Theor Appl Fract Mech 129:104208. https://doi.org/10.1016/j.tafmec.2023.104208

Chang X, Zhang X, Qian LZ et al (2022) Influence of bedding anisotropy on the dynamic fracture behavior of layered phyllite. Eng Fract Mech 260:108183. https://doi.org/10.1016/j.engfracmech.2021.108183

Chen BL, Xie LZ, Zhang Y et al (2023) Study on the developmental characteristics and mechanism of shale FPZs. Theor Appl Fract Mech 124:103814. https://doi.org/10.1016/j.tafmec.2023.103814

Dong LJ, Yang LB, Chen YC (2022) Acoustic emission location accuracy and spatial evolution characteristics of granite fracture in complex stress conditions. Rock Mech Rock Eng 56:1113–1130. https://doi.org/10.1007/s00603-022-03124-y

Du K, Li XF, Tao M et al (2020) Experimental study on acoustic emission (AE) characteristics and crack classification during rock fracture in several basic lab tests. Int J Rock Mech Min Sci 133:104411. https://doi.org/10.1016/j.ijrmms.2020.104411

Ersoy H, Karahan M, Kolayli H et al (2021) Influence of mineralogical and micro-structural changes on the physical and strength properties of post-thermal-treatment clayed rocks. Rock Mech Rock Eng 54:679–694. https://doi.org/10.1007/s00603-020-02282-1

Fan ZD, Xie HP, Zhang R et al (2022) Characterization of anisotropic mode II fracture behaviors of a typical layered rock combining AE and DIC techniques. Eng Fract Mech 271:108599. https://doi.org/10.1016/j.engfracmech.2022.108599

Feng G, Wang XC, Wang M et al (2020) Experimental investigation of thermal cycling effect on fracture characteristics of granite in a geothermal-energy reservoir. Eng Fract Mech 235:107180. https://doi.org/10.1016/j.engfracmech.2020.107180

Ghazvinian A, Vaneghi RG, Hadei MR et al (2013) Shear behavior of inherently anisotropic rocks. Int J Rock Mech Min Sci 61:96–110. https://doi.org/10.1016/j.ijrmms.2013.01.009

Hanano M (2004) Contribution of fractures to formation and production of geothermal resources. Renew Sustain Energy Rev 8:223–236. https://doi.org/10.1016/j.rser.2003.10.007

Hargraves RB, Johnson D, Chan CY (1991) Distribution anisotropy: the cause of AMS in igneous rocks? Geophys Res Lett 18:2193–2196. https://doi.org/10.1029/91GL01777

Jiang Y, Su HJ, Zhang LQ et al (2023) Heating-path dependency of fracture behavior of sandstone subjected to thermal treatment. Theor Appl Fract Mech 127:104096. https://doi.org/10.1016/j.tafmec.2023.104096

Jiang TQ, Zhu C, Qiao Y et al (2024) Deterioration evolution mechanism and damage constitutive model improvement of sandstone-coal composite samples under the effect of repeated immersion. Phys Fluids 36:056611. https://doi.org/10.1063/5.0208619

Jiang TQ, Cao XX, Duan HY et al (2025) Recycling efficiency mechanism of recycled concrete aggregate to improve the CO_2 uptake and anti-leakage properties of CO_2 sequestration functional backfills. Constr Build Mater 458:139663. https://doi.org/10.1016/j.conbuildmat.2024.139663

Karimi F, Mousavi SR, Miri M (2024) Tensile-Tear cracking resistance of RAP incorporated asphalt mixtures, enhanced by warm mix asphalt additive and nano calcium carbonate. Theor Appl Fract Mech 132:104467. https://doi.org/10.1016/j.tafmec.2024.104467

Landau HJ (1967) Sampling, data transmission, and the Nyquist rate. Proc IEEE 55:1701–1706. https://doi.org/10.1109/proc.1967.5962

Li SL, Wu YQ, Shi HS (2019) A novel acoustic emission monitoring method of cross-section precise localization of defects and wire breaking of parallel wire bundle. Struct Control Health Monit 26:e2334. https://doi.org/10.1002/stc.2334

Liu T, Han C, Wang QL et al (2022) A method of acoustic emission source location for engine fault based on time difference matrix. Struct Health Monit 22:621–638. https://doi.org/10.1177/14759217221088995

Liu ZL, Ma CD, Wei XA (2023) Study on fracture behavior of layered limestone under mixed mode I/III loading. Theor Appl Fract Mech 128:104102. https://doi.org/10.1016/j.tafmec.2023.104102

Liu KW, Zou LS, Guo TF et al (2024) Fracture behavior and acoustic emission characteristics of layered sandstone with a bedding-parallel crack. Theor Appl Fract Mech 131:104344. https://doi.org/10.1016/j.tafmec.2024.104344

Ma TS, Wang HA, Liu Y et al (2023) Experimental investigation on the anisotropy of mode-I fracture and tensile failure of layered shale. Eng Fract Mech 290:109484. https://doi.org/10.1016/j.engfracmech.2023.109484

Miao ST, Pan PZ, Yu PY et al (2020) Fracture analysis of Beishan granite after high-temperature treatment using digital image correlation. Eng Fract Mech 225:106847. https://doi.org/10.1016/j.engfracmech.2019.106847

Min KB, Rutqvist J, Tsang CF, Jing L (2005) Thermally induced mechanical and permeability changes around a nuclear waste repository—a far-field study based on equivalent properties determined by a discrete approach. Int J Rock Mech Min Sci 42:765–780. https://doi.org/10.1016/j.ijrmms.2005.03.014

Nejati M, Paluszny A, Zimmerman RW (2015) On the use of quarter-point tetrahedral finite elements in linear elastic fracture mechanics. Eng Fract Mech 144:194–221. https://doi.org/10.1016/j.engfracmech.2015.06.055

Nejati M, Bahrami B, Ayatollahi MR et al (2021) On the anisotropy of shear fracture toughness in rocks. Theor Appl Fract Mech 113:102946. https://doi.org/10.1016/j.tafmec.2021.102946

Pietras D, Aliha MRM, Kucheki HG et al (2023) Tensile and tear-type fracture toughness of gypsum material: Direct and indirect testing methods. J Rock Mech Geotech Eng 15:1777–1796. https://doi.org/10.1016/j.jrmge.2022.11.016

Ren L, Xie HP, Sun X et al (2021) Characterization of anisotropic fracture properties of silurian longmaxi shale. Rock Mech Rock Eng 54:665–678. https://doi.org/10.1007/s00603-020-02288-9

Ren FQ, Zhu C, Yuan ZH et al (2023) Recognition of shear and tension signals based on acoustic emission parameters and waveform using machine learning methods. Int J Rock Mech Min Sci 171:105578. https://doi.org/10.1016/j.ijrmms.2023.105578

Roy DG, Singh TN, Kodikara J (2017) Influence of joint anisotropy on the fracturing behavior of a sedimentary rock. Eng Geol 228:224–237. https://doi.org/10.1016/j.enggeo.2017.08.016

Saceanu MC, Paluszny A, Zimmerman RW et al (2022) Fracture growth leading to mechanical spalling around deposition boreholes of an underground nuclear waste repository. Int J Rock Mech Min Sci 152:105038. https://doi.org/10.1016/j.ijrmms.2022.105038

Sakha M, Nejati M, Aminzadeh A et al (2022) On the validation of mixed-mode I/II crack growth theories for anisotropic rocks. Int J Solids Struct 241:111484. https://doi.org/10.1016/j.ijsolstr.2022.111484

Shang JL, Jayasinghe LB, Xiao F et al (2019) Three-dimensional DEM investigation of the fracture behaviour of thermally degraded rocks with consideration of material anisotropy. Theor Appl Fract Mech 104:102330. https://doi.org/10.1016/j.tafmec.2019.102330

Shen YJ, Hou X, Yuan JQ et al (2020) Thermal deterioration of high-temperature granite after cooling shock: Multiple-identification and damage mechanism. Bull Eng Geol Environ 79:5385–5398. https://doi.org/10.1007/s10064-020-01888-7

Shi XS, Zhao YX, Gong S et al (2022) Co-effects of bedding planes and loading condition on Mode-I fracture toughness of anisotropic rocks. Theor Appl Fract Mech 117:103158. https://doi.org/10.1016/j.tafmec.2021.103158

Shi ZM, Li JT, Wang MX et al (2023) Effect of temperature on pure mode III fracture behavior and fracture morphology of granite after thermal shock. Theor Appl Fract Mech 127:104024. https://doi.org/10.1016/j.tafmec.2023.104024

Shi ZM, Li JT, Ranjith PG et al (2024) Acoustic emission and fracture morphology characteristics of thermal-damage granite under mixed mode I/III loading. Theor Appl Fract Mech 133:104524. https://doi.org/10.1016/j.tafmec.2024.104524

Shui X, Zhou L, Zhu ZM et al (2024) Investigation of the fracture characteristics of mixed-mode I/III crack by using two kinds of sandstone specimens. Eng Fract Mech 310:110488. https://doi.org/10.1016/j.engfracmech.2024.110488

Su HJ, Qin XF, Feng YJ et al (2022) Experimental investigation of mixed mode I-II fracture property of thermally treated granite under dynamic loading. Theor Appl Fract Mech 118:103267. https://doi.org/10.1016/j.tafmec.2022.103267

Sun Z, Zhao YX, Gao YR et al (2024) Effect of size and anisotropy on mode I fracture toughness of coal. Theor Appl Fract Mech 129:104170. https://doi.org/10.1016/j.tafmec.2023.104170

Suo Y, Chen ZX, Rahman SS et al (2020) Experimental and numerical investigation of the effect of bedding layer orientation on fracture toughness of shale rocks. Rock Mech Rock Eng 53:3625–3635. https://doi.org/10.1007/s00603-020-02131-1

Ulusay R (2015) The ISRM suggested methods for rock characterization, testing and monitoring: 2007–2014. Springer, Cham. https://doi.org/10.1007/978-3-319-07713-0

Wang H, Li Y, Cao SG et al (2020) Fracture toughness analysis of HCCD specimens of Longmaxi shale subjected to mixed mode

I-II loading. Eng Fract Mech 239:107299. https://doi.org/10.1016/j.engfracmech.2020.107299
Wang W, Wang CL, Zhao Y et al (2024) Study on I/III mixed fracture characteristics of coal in different regions of China. Theor Appl Fract Mech 134:104712. https://doi.org/10.1016/j.tafmec.2024.104712
Weng MC, Lin SS, Lee CS et al (2024) An anisotropic thermal-mechanical coupling failure criterion for slate. Rock Mech Rock Eng 57:8157–8177. https://doi.org/10.1007/s00603-024-03992-6
Wong LNY, Zhang YH, Wu ZJ (2020) Rock strengthening or weakening upon heating in the mild temperature range? Eng Geol 272:105619. https://doi.org/10.1016/j.enggeo.2020.105619
Xi Y, Wang HY, Zhang H et al (2024) Effects of different bedding angles and impact angles on the dynamic tensile properties of thermal-treated shale after cooling treatment. Rock Mech Rock Eng 57:8457–8481. https://doi.org/10.1007/s00603-024-03973-9
Xia BW, Li Y, Hu HR et al (2022) Effect of crack angle on mechanical behaviors and damage evolution characteristics of sandstone under uniaxial compression. Rock Mech Rock Eng 55:6567–6582. https://doi.org/10.1007/s00603-022-03016-1
Yang Z, Tao M, Fei WB et al (2024) A coupled thermo-mechanical model for investigating cracking and failure of composite interbedded rock. Eng Geol 339:107645. https://doi.org/10.1016/j.enggeo.2024.107645
Yin TB, Li XB, Xia KW et al (2012) Effect of thermal treatment on the dynamic fracture toughness of Laurentian granite. Rock Mech Rock Eng 45:1087–1094. https://doi.org/10.1007/s00603-012-0240-3
Yin TB, Tan XS, Wu Y et al (2021) Temperature dependences and rate effects on mode II fracture toughness determined by punch-through shear technique for granite. Theor Appl Fract Mech 114:103029. https://doi.org/10.1016/j.tafmec.2021.103029
Zeng LB, Zhao JY, Zhu SJ et al (2008) Impact of rock anisotropy on fracture development. Prog Nat Sci 18:1403–1408. https://doi.org/10.1016/j.pnsc.2008.05.016
Zhao YX, Liu B (2021) Deformation field and acoustic emission characteristics of weakly cemented rock under Brazilian splitting test. Nat Resour Res 30:1925–1939. https://doi.org/10.1007/s11053-020-09809-x
Zhao WC, Wang ZZ, Song ZL et al (2021) Experimental exploration of damage propagation in rocks using acoustic emission. Bull Eng Geol Environ 80:6065–6075. https://doi.org/10.1007/s10064-021-02325-z
Zhao Y, Yuan YL, Wang CL et al (2024a) The mode I fracture toughness and acoustic emission characteristics of hot dry rock under temperature effects. Eng Fract Mech 301:110047. https://doi.org/10.1016/j.engfracmech.2024.110047
Zhao ZH, Chen SS, Zhang JT et al (2024b) In-situ tracer test in fractured rocks for nuclear waste repository. Earth Sci Rev 250:104683. https://doi.org/10.1016/j.earscirev.2024.104683
Zheng K, Wang CL, Zhao Y et al (2023a) Assessment on anisotropy degree and fracture modes for weakly anisotropic sandstone using the acoustic emission technique. Fatigue Fract Eng Mater Struct 46:2766–2783. https://doi.org/10.1111/ffe.14031
Zheng K, Wang CL, Zhao Y et al (2023b) Theoretical and experimental exploration on the combined mode I+III fracture toughness of shale using the edge-notched disk bending method with acoustic emission monitoring. Theor Appl Fract Mech 125:103870. https://doi.org/10.1016/j.tafmec.2023.103870
Zheng K, Wang CL, Zhao Y et al (2024) A modified 3D mean strain energy density criterion for predicting shale mixed-mode I/III fracture toughness. J Rock Mech Geotech Eng 16:2411–2428. https://doi.org/10.1016/j.jrmge.2023.09.016
Zhou Q, Xie HP, Zhu ZM et al (2023) Fracture toughness anisotropy in shale under deep in situ stress conditions. Rock Mech Rock Eng 56:7535–7555. https://doi.org/10.1007/s00603-023-03454-5
Zhou PL, Xie HP, Wang J et al (2024) Thermal effects on mechanical and failure behaviors of anisotropic shale subjected to direct shear. J Rock Mech Geotech Eng. https://doi.org/10.1016/j.jrmge.2024.05.032
Zhuang L, Zang A (2021) Laboratory hydraulic fracturing experiments on crystalline rock for geothermal purposes. Earth Sci Rev 216:103580. https://doi.org/10.1016/j.earscirev.2021.103580